# Explicit implementation of hydrogen transport in metals

A. Díaz [a,*], J.M. Alegre [a], I.I. Cuesta [a], Z. Zhang [b]

[a] *Universidad de Burgos, Escuela Politécnica Superior, Avenida Cantabria s/n, Burgos 09006, Spain*
[b] *Department of Structural Engineering, Norwegian University of Science and Technology (NTNU), Trondheim 7491, Norway*

## ARTICLE INFO

## ABSTRACT

Hydrogen embrittlement prediction demands a numerical framework coupling a damage model with local hydrogen concentration. The inherent nonlinearity in hydrogen-stress-damage interactions challenges convergence in implicit schemes. To address this limitation, we propose a novel chemical potential-based explicit formulation for simulating hydrogen transport in metals. Our approach exploits a heat transfer analogy, linking mechanical and hydrogen transport *via* inelastic energy as a heat source. By employing chemical potential rather than lattice concentration, our method eliminates the need for user-defined boundary conditions and hydrostatic stress gradient determination. We integrate a VUMATHT subroutine for diffusion modelling and a VUMAT subroutine for material behaviour, coupling stress and strain rates as a heat source for diffusion. Validating against a classical benchmark, we compare our explicit approach with hydrogen concentration-based methods in ABAQUS Standard and Comsol Multiphysics. Stability conditions are assessed for different mesh sizes and mass scaling densities and the capabilities of our approach are showcased for 3D simulations of notched tensile specimens. Our framework offers a novel and efficient pathway for integrating hydrogen transport with user-defined material behaviour, promising advancements in hydrogen-informed damage models.

## 1. Introduction

Hydrogen embrittlement (HE) is a degradation process suffered by many metals and alloys and limits material selection for H-producing environments [1]. This phenomenon also hinders a cost-effective hydrogen transport and storage and thus the adoption of $H_2$ as an energy carrier [2]. Challenges that are encountered for the prevention or mitigation HE are numerous. The operating micro-mechanisms are not yet completely understood. Experimental and theoretical evidence has been given to support different micro-mechanisms, e.g. hydrogen-enhanced decohesion (HEDE) [3,4], hydrogen-enhanced localised plasticity (HELP) [5,6] or adsorption-induced dislocation emission (AIDE) [7,8], but the predominance of a mechanism can usually be only speculated due to the complex hydrogen-microstructure interaction. One of the reasons for the elusive nature of HE is the difficulty in hydrogen mapping within the microstructure and near cracks or defects [9]. In addition, testing procedures to characterise HE include a wide range of charging methods and conditions and therefore the reproducibility and transferability is limited. As a consequence, design criteria are conservative and some HE tests are only valid as screening methods [10]. Within this context, the role of numerical modelling in explaining hydrogen accumulation and damage is crucial both for the elucidation of HE micro-mechanisms and for the improvement of design criteria.

A modelling framework must include the following ingredients to comprehensively capture HE: (i) damage modelling to predict crack nucleation and propagation; (ii) a local reduction of fracture properties as a function of hydrogen concentration; (iii) a microstructure-informed transport model that includes stress-assisted hydrogen diffusion and trapping. The present paper focuses on the last ingredient and proposes a novel modelling strategy to couple hydrogen transport to damage models that suffer from convergence issues.

Explicit schemes to simulate failure have been considered for GTN (Gurson–Tvergaard–Needleman) [11,12], CZ (cohesive zone) [13,14] or PF (phase field) [15,16] modelling approaches. The need of this explicit formulation has been discussed by different authors. Within the framework of continuum damage mechanics (CDM), Zhou et al. (2017) [17] implemented a viscoplastic damage model using a VUMAT in ABAQUS Explicit to simulate a Nakajima test, i.e. a hot stamping test. They justified the use of an explicit scheme to avoid the update of the tangent matrix and to capture the contact-friction phenomenon due to the small time steps. Lemaitre ductile damage model, a widely used CDM model,

has also been implemented in ABAQUS Explicit through VUMAT subroutines for piercing or forming simulations [18–20].

Phase field models for fracture are also characterised by slow convergence rates during unstable crack propagation, especially for staggered schemes [21]. Despite the popularity of PF to simulate fracture, the extremely high number of degrees of freedoms due to small regularization lengths or in 3D models hinders the applicability to real components. For that reason, VUMAT implementation in ABAQUS Explicit has been developed by Hai et al. (2024) [22] for quasi-static PF problems in 3D to overcome the vast number of iterations of implicit schemes. To ensure a quasi-static response using explicit schemes, loading times need to be long enough. Other authors have used explicit schemes for dynamic PF [23] and for composite PF fracture [24]. Explicit integration in PF also avoids the determination of the second derivative of the energy functional that is required in the implicit formulation [23]. Explicit time integration also facilitates parallel computing strategies to improve computational efficiency, as demonstrated by Wang et al. (2019) [25] for dynamic and quasi-static PF in 3D problems. Ziaei-Rad and Shen (2016) [26] also showed that explicit time integration is advantageous for GPU parallelization of rate-dependent phase field problems.

Hydrogen-informed damage models are increasingly being proposed, including Gurson-based models [27,28], cohesive zone models [29–31] and phase field fracture models [32–34]. Hydrogen degradation is included as a phenomenological or mechanistic expression within these modelling frameworks. For example, Gurson-based models have been proposed to capture hydrogen-void interactions [27,35], which are involved in HELP and HESIV (hydrogen-enhanced strain-induced vacancy formation) mechanisms. Cohesive zone and phase field models are sometimes informed by atomistic simulations of hydrogen-enhanced decohesion [36,37] but can also be fitted from experimental tests [38, 39].

However, the lack of an explicit implementation of hydrogen transport models is limiting the application of existing damage subroutines to hydrogen-assisted fracture models. Therefore, the main purpose of the present strategy, and the corresponding developed subroutines, is to inform the vast amount of damage models in literature that are based on ABAQUS Explicit.

With the aim of solving the coupled hydrogen transport problem, an implementation strategy in ABAQUS Explicit is presented here considering a VUMATHT subroutine that is informed by the stress and strain coupled effects from a VUMAT subroutine. The inverse route, i.e. that hydrogen concentration informs the material constitutive behaviour, is also possible through the present framework.

The strategy here adopted follows the heat transfer analogy commonly exploited, but in this case a heat source from the dissipated inelastic energy is assumed as the link between mechanical and hydrogen transport problems. In addition, the chemical potential is the governing degree of freedom instead of the lattice concentration. The advantages of this approach were already mentioned by Di Leo & Anand (2013) [40] and are particularised for the implementation in ABAQUS through heat transfer analogies:

- *User-defined boundary conditions are not needed to capture the stress-dependent entry.* Applying the heat transfer analogy to a concentration-based implementation, a user-defined temperature can be defined on surface nodes using a DISP subroutine [41], but the stress nodal values should be extrapolated and averaged from integration points. A chemical potential boundary condition circumvents this operation.
- *The determination of hydrostatic stress gradients is not required.* This is the crucial advantage that suggests that the chemical potential-based formulation is a feasible alternative for Explicit implementation. Access to neighbour integration points is carried out in previous ABAQUS Standard approaches [41,42], but this is not straightforward in Explicit, as detailed in Sections 2 and 3.

Regarding the first advantage, it is important to highlight that the stress influence on hydrogen uptake is usually overlooked in literature on HE. Modelling frameworks for hydrogen adsorption/absorption are usually reaction-based for electrochemical charging [43–45] whereas gaseous uptake is traditionally modelled by chemical potentials in equilibrium [46]. Equivalence between both charging methods requires further research [47] and can foster simplified electrochemical testing methods to avoid costly high-pressure facilities.

The simplest boundary condition for hydrogen transport models is a constant concentration, which is derived from the Sievert's law for gaseous hydrogen uptake. Surface concentration is found to follow a square root function of the $H_2$ pressure. This relationship is determined by the equilibrium between the chemical potential of hydrogen in solid solution ($\mu_L$) and the adsorbed hydrogen, ($1/2\mu_{H_2}$) [46]. However, when the reduction of $\mu_L$ due to the hydrostatic stress is taken into account a stress-dependent solubility is obtained [40]. Modelling features for uptake in representative works for hydrogen transport near a crack tip are summarised in Table 1. Many works consider a constant boundary concentration, $C_L^B = C_L^0 = K\sqrt{p_{H_2}}$, following the seminar work of Sofronis & McMeeking [48], where $K$ is the solubility and $p_{H_2}$ the $H_2$ pressure. However, as demonstrated by Di Leo & Anand [40], the neglection of stress effects on $C_L^B$ results in distributions that are not coherent with the steady state. The physically based uptake and the corresponding stress effect can be modelled both in a chemical potential-based formulation [40] or applying a boundary concentration with an exponential term including the hydrostatic stress $\sigma_h$ [41,49]. Both formulations will be extended in Section 2. An important implication of the hydrostatic stress influence on hydrogen uptake is the need of accurate stress determination at a notch or crack tip. Classical plasticity, e.g. J2 Von-Mises plasticity, is usually assumed but conventional theories do not capture size effects at the micron scale. To overcome this limitation, Pañeda et al. [37,49] have explored the influence of strain gradient plasticity (SGP) on hydrostatic stress values at a crack tip and thus on hydrogen uptake. The high stress values predicted by SGP suggest that hydrogen transport models coupled to classical plasticity could be critically underestimating

**Table 1**

*Summary of relevant approaches for modelling hydrogen uptake on a crack surface. The simpler constant concentration assumption does not capture the stress dependency and must be replaced by a concentration boundary condition with an exponential term including the hydrostatic stress. This approach might also be considered in a flux-based boundary condition. Di Leo & Anand proposed instead the use of the chemical potential as the diffusion governing variable, circumventing the need of stress-dependent boundary conditions.*

| Refs. | Boundary condition for hydrogen uptake | Implications |
|---|---|---|
| Sofronis &McMeeking [48], Krom et al. [54], Dadfarnia et al. [55], Kotake [56]. | $C_L^B = C_L^0 = K\sqrt{p_{H_2}}$ | Steady state is not coherent with $C_L$ distributions after long diffusion times. |
| Di Leo & Anand [40] | $\mu_L^B = \mu_L^0 = \frac{1}{2}\mu_{H_2}$ | Based on thermodynamics and consistent with steady state. Stress-enhanced uptake is naturally captured. |
| Díaz et al. [41] | $C_L^B = C_L^0 \exp\left(\frac{\overline{V}_H \sigma_h^B}{RT}\right)$ | Stress-enhanced uptake is modelled by boundary condition depending on $\sigma_h$. |
| Pañeda et al. [49] | $C_L^B = C_L^0 \exp\left(\frac{\overline{V}_H \sigma_{h,SGP}^B}{RT}\right)$ | Prediction of very high $\sigma_{h,SGP}^B$, and thus $C_L^B$, values. |
| Turnbull et al. [52] Pañeda et al. [53] | $J_L^B = k_{abs}\exp\left(\frac{\overline{V}_H \sigma_h^B}{RT}\right)\theta_{ad} - k_{des}C_L^B(1 - \theta_{ad})$ | Reaction-based boundary condition derived from hydrogen evolution reaction (adsorption) and absorption/desorption kinetics. |

the surface concentration.

Boundary conditions to capture electrochemical hydrogen adsorption are based on hydrogen evolution reaction (HER) theory. The validity of constant concentration or constant flux boundary conditions depends on the reaction mechanism, as discussed by Montella et al. [50] for potentiostatic or galvanostatic charging. A generalised flux $J_L^B$ that evolves with the surface coverage of adsorbed hydrogen ($\theta_{ad}$) and with the boundary lattice concentration, $C_L^B$, was derived by Turnbull et al. for hydrogen uptake at a crack tip from the imbalance between adsorption, absorption and diffusion fluxes [44,51,52]. This approach was also implemented by Pañeda et al. [53], including the SGP effects.

In the present work, reaction-based boundary conditions are not addressed, and the discussion is restricted to constant concentration and constant chemical potential assumptions. Four strategies to implement a hydrogen transport model are presented, as summarised in Table 2, but the focus is put on details about the Explicit approach in ABAQUS due to the limitations of explicit subroutines to mimic Implicit implementations. A novel procedure is here proposed based on the combination of a VUMATHT, where the diffusion equation is modelled through a heat transfer analogy, and a VUMAT in which material modelling is defined and the coupling stress and strain rate terms are stored and passed as a heat source to the diffusion problem.

It is important to emphasise that the chemical potential-based implementation in ABAQUS Explicit that is here proposed is not aimed at circumventing convergence issues of hydrogen transport simulations. The present work extends the applicability of the heat transfer analogy developed in Díaz et al. (2016) and proposes a framework to be easily coupled with damage models in future research.

The development of Di Leo & Anand (2013) [40] for a chemical potential-based hydrogen transport model is followed in the present work and is presented in Section 2. That section also revisits the concentration-based implementation in ABAQUS Standard and both concentration and chemical-potential based implementation through custom PDEs in Comsol Multiphysics. The detailed procedure to model coupled hydrogen transport in ABAQUS Explicit is described in Sections 3 and 4, and later verified using a 2D boundary layer model in Section 5. The ability to capture strain rate effects and the accuracy of predictions are compared against other user-defined implicit schemes. The applicability of the proposed computational procedure for 3D simulations is demonstrated and discussed in Section 6, comparing the accuracy and efficiency of different elements. Finally, the sensitivity of the model to mass scaling and mesh size is studied for a axisymmetric model in Section 7.

## 2. Hydrogen transport modelling

Hydrogen transport equations based on the concentration or on the chemical potential as dependent variables are presented in this section. However, basic mathematical derivations are detailed in Appendices B and C. The list of symbols used through the text is included in Appendix A. A complete coupled chemo-mechanical formulation is not detailed, and the focus is put on the mass balance governing hydrogen diffusion.

**Table 2**

*A hydrogen transport modelling framework is developed in ABAQUS Explicit (\*E) using VUMATHT and VUMAT subroutines. This approach is validated by comparing results with other implicit (\*I) implementations in ABAQUS and Comsol Multiphysics, considering both governing balances based on the lattice concentration or on the chemical potential.*

| | Concentration balance ($C_L$) | Chemical potential balance ($\mu_L$) |
|---|---|---|
| ABAQUS user-defined subroutines | UMATHT (\*I) | **VUMATHT + VUMAT** (\*E) |
| Comsol Multiphysics PDEs | Diffusion-convection-reaction PDE (\*I) | Diffusion-reaction PDE (\*I) |

The formulation elaboration follows mainly the framework established by Sofronis & McMeeking (1989) [48] to expand a modified mass balance and by Di Leo & Anand (2013) [40] to derive a chemical potential-based transport equation.

Hydrogen transport refers here to the comprehensive process of hydrogen uptake from the environment (boundary conditions), hydrogen diffusion produced by chemical gradients (mass flux and balance) and hydrogen trapping in microstructural defects (modification of mass balance). Non-interstitial transport mechanisms as grain boundary diffusion [57] or transport by dislocations [58] can be easily accommodated in the present framework.

The considered framework has its origin in the partition of hydrogen concentration into two species to account for trapping effects, i.e. a two-level approach where hydrogen in lattice sites (L subscript) and in trapping sites (T subscript) are considered two diffusing species. This framework could be easily extended to multiple trapping sites [42,55,59]. Alternatives to the discrete modelling of trapping sites, e.g. non-uniform diffusion and solubility models, are discussed by Toribio & Kharin (2015) [60] within a general diffusion-trapping framework. Neglecting the flux between traps, the mass balance can be expressed as:

$$\frac{\partial C_L}{\partial t} + \frac{\partial C_T}{\partial t} = -\nabla \cdot \mathbf{J}_L \tag{1}$$

where, $C_L$ and $C_T$ are hydrogen concentrations in lattice and trapping sites, respectively, and $\mathbf{J}_L$ represents a hydrogen flux vector. Assuming classical diffusion, flux of hydrogen through lattice sites is proportional to a lattice diffusion coefficient, $D_L$, and to the concentration gradient:

$$\mathbf{J}_L = -D_L \nabla C_L \tag{2}$$

However, in the context of a generalised thermodynamic forces [61], the gradient of the chemical potential of hydrogen in lattice sites, $\mu_L$, drives diffusion. This approach accounts implicitly for temperature or pressure gradient effects:

$$\mathbf{J}_L = -D_L \frac{C_L}{RT} \nabla \mu_L \tag{3}$$

where, $R$ is the constant of gases and $T$ the temperature. For solute hydrogen and considering only a dilatational influence of hydrostatic stress, the chemical potential of lattice hydrogen can be expressed as follows [62,63]:

$$\mu_L = \mu_L^0 + RT \ln\left(\frac{C_L}{N_L - C_L}\right) - \overline{V}_H \sigma_h \tag{4}$$

The last term in Eq. (4) captures the reduction in the chemical potential in tensile regions and it is proportional to the hydrostatic stress, $\sigma_h$, and to the partial molar volume of hydrogen in the metal, $\overline{V}_H$, which can be experimentally measured [64]. The influence of a non-isotropic expansion terms and asymmetrical strain fields in the chemical potential has been discussed by other authors [65,66]. *Ab initio* calculations of the hydrostatic and anisotropic stress influence on hydrogen diffusion are also found in literature [67]. The present model is restricted to the simple $\overline{V}_H \sigma_h$ form as a drift diffusion term. For alloys with a low hydrogen solubility a low occupancy is always assumed, i.e., $C_L \ll N_L$ or $\theta_L \ll 1$, where $\theta_L$ is defined as $C_L/N_L$. Thus, the chemical potential expression can be simplified:

$$\mu_L = \mu_L^0 + RT \ln\left(\frac{C_L}{N_L}\right) - \overline{V}_H \sigma_h \tag{5}$$

### 2.1. Concentration-based modelling

The derivation of the governing equation based on the lattice concentration as dependent variable is detailed in Appendix B. It is important to note that thermodynamic equilibrium, the so-called Oriani's equilibrium [68], has been assumed here between lattice and

trapped hydrogen. For the sake of generalisation, kinetic exchange between both residing sites has been included in the two-level model following the formulation from McNabb & Foster (1963) [69]. Kinetic trapping are not addressed in the present work but discussions about the conditions for equilibrium validity can be found in literature [70–73]. From the implementation perspective, the strategy proposed in the present paper can easily be extended to the McNabb & Foster's formulation following an analytic approximation [74]. For an isothermal analysis where temperature $T = T_0$ is constant and uniform, the governing equation for the concentration-based model is:

$$\left(1 + \frac{C_T(1 - \theta_T)}{C_L}\right)\frac{\partial C_L}{\partial t} + \theta_T\frac{\partial N_T}{\partial \varepsilon_p}\frac{\partial \varepsilon_p}{\partial t} = \nabla\cdot\left(D_L\nabla C_L - \frac{D_L C_L}{RT_0}\overline{V}_H\nabla\sigma_h\right) \quad (6)$$

The term multiplying $\partial C_L/\partial t$ represents a numerical damping or, in analogy with a heat transfer problem, a specific heat term. This term can be defined as $D_L/D_{eff}$ [48] where the effective or operational diffusivity quantifies the local deviation from ideal diffusion. Here, $D_L/D_{eff}$ is simply termed as a non-dimensional factor $D^*$ [40]:

$$D^*\frac{\partial C_L}{\partial t} + \theta_T\frac{\partial N_T}{\partial \varepsilon_p}\frac{\partial \varepsilon_p}{\partial t} = \nabla\cdot\left(D_L\nabla C_L - \frac{D_L C_L}{RT_0}\overline{V}_H\nabla\sigma_h\right) \quad (7)$$

This coefficient $D^*$ can be rearranged to be expressed only as a function of the dependent variable, $C_L$, and of material parameters, $N_L$, $N_T$ and $K_T = \exp(E_B/RT)$:

$$D^* = 1 + \frac{K_T N_T/N_L}{\left(1 + K_T C_L/N_L\right)^2} \quad (8)$$

In addition, as shown in Eq. (6), a sink or source term needs to be included in the implementation to account for the plastic strain rate influence. Since this term was firstly proposed and discussed by Krom et al. (1999) [54], it is referred as Krom's term. These authors demonstrated that if this term is not considered, hydrogen depletion from lattice due to fast trapping creation is not captured. In that case, hydrogen is artificially created and the mass balance is not verified.

As previously discussed, boundary conditions for the hydrogen transport equation are typically based on constant concentration to capture hydrogen uptake. Zero-concentration and zero-flux boundary conditions are also used to simulate hydrogen exit or insulation, respectively. The chemical potential is the general thermodynamic variable driving diffusion (Eq. (3)), but also needs to be considered for equilibrium with the environment [46]. As elaborated in Section 3.3, the equilibrium condition of lattice sites with gaseous hydrogen results in a stress-dependent boundary condition $C_L^B$:

$$C_L^B = C_L^0\exp\left(\frac{\overline{V}_H\sigma_h^B}{RT}\right) \quad (9)$$

where, $C_L^0$ represents a concentration in equilibrium with the environment in the absence of stress and $\sigma_h^B$ is the hydrostatic stress value at the boundary.

### 2.1.1. ABAQUS standard

The concentration-based governing Eq. (7) has been successfully implemented in ABAQUS Standard following a heat transfer analogy through a user subroutine UMATHT. One of the critical aspects is the calculation of $\nabla\sigma_h$ that modifies the flux expression through the drifted diffusion term. Díaz et al. (2016) [41] combined a USDFLD subroutine, to access $\sigma_h$ values at the material points, with a UMATHT where the gradient of the stored values is calculated considering an isoparametric formulation. This approach can be used with the built-in elastoplastic models and was validated with CPE8RT elements, i.e. plane strain elements with 8 nodes and reduced integration. On the other hand, Férnandez-Sousa et al. (2020) [42] directly determine $\nabla\sigma_h$ within a UMAT in which a user-defined material constitutive behaviour is modelled. In both approaches, $\sigma_h$ values must be stored in order to access

to the values at all the integration points within an element. As pointed out by Hageman & Pañeda (2023) [75], the second-order derivatives for $\sigma_h$ are poorly defined using quadratic elements with C0 continuity but hydrostatic stress distribution can be accurately captured if a sufficiently fine mesh is considered.

Access to the equivalent plastic strain at integration points is also needed to calculate $N_T$ and the equivalent plastic strain rate to include Krom's term in the mass balance. It is also important to consider that UMAT or USDFLD are called before the UMATHT in the ABAQUS internal calling sequence. Therefore, variable updates and subroutine call order must be carefully considered to avoid undesired staggered solutions. The separated or fully coupled nature of the coupled temperature-displacement problem can be controlled through ABAQUS solution methods.

To model the governing Eq. (7) in a UMATHT in ABAQUS Standard, the total concentration, $C_L + C_T$, is considered as the internal thermal energy $U$. Therefore, the term $D^*$ can be assigned to the specific heat term $\partial U/\partial T$:

$$\underbrace{D^*}_{\partial U/\partial T}\frac{\partial C_L}{\partial t} + \theta_T\underbrace{\frac{\partial N_T}{\partial \varepsilon_p}\frac{\partial \varepsilon_p}{\partial t}}_{dU_p} = \nabla\cdot\left(\underbrace{D_L\nabla C_L - \frac{D_L C_L}{RT_0}\overline{V}_H\nabla\sigma_h}_{\mathbf{J}_L}\right) \quad (10)$$

A numerical density equal to 1 is fixed for the heat thermal problem and it is thus omitted in the specific heat term. This unitary value must not be confused with the material numerical density for the Explicit problem, whose value is modified to tune mass scaling. The energy to be updated at the end of the increment, i.e. at $n + 1$, represents the total concentration and therefore the Krom's term, which represents the contribution of trap creation during plastic straining, $dU_p$, is included:

$$U^{n+1} = U^n + \frac{\partial U}{\partial T}dC_L + dU_p \quad (11)$$

It must be noted that $C_L$ is stored as the temperature degree of freedom and therefore $dC_L$ is accessed directly as DTEMP. Similarly, the implemented flux term uses the available DTEMDX, i.e. $\nabla C_L$, and the $\nabla\sigma_h$ term calculated using an internal isoparameteric derivation as detailed in Ref. [41].

The stress-dependent boundary condition, $C_L^B$, that is required for thermodynamic consistency (Section 3.3) is implemented in ABAQUS Standard using a DISP subroutine for the temperature degree of freedom and averaging hydrostatic stress values at the boundary nodes [41].

### 2.1.2. Comsol multiphysics

The implementation of Eq. (7) in Comsol Multiphysics can be performed using the *Stabilized convection-diffusion equation* as a PDE to be coupled with the *Solid Mechanics* module. The built-in physics interfaces facilitate the assignment and coupling of terms without coding. For hydrogen transport modelling, a source term ($f$), damping ($d_a$), diffusion ($D_L$) and conservative convection coefficients ($\alpha$) are correspondingly defined.

$$\underbrace{D^*}_{d_a}\frac{\partial C_L}{\partial t} + \nabla\cdot\left(-D_L\nabla C_L + \underbrace{C_L\frac{D_L}{RT_0}\overline{V}_H\nabla\sigma_h}_{\alpha}\right) = \underbrace{\theta_T\frac{\partial N_T}{\partial \varepsilon_p}\frac{\partial \varepsilon_p}{\partial t}}_{f} \quad (12)$$

Hydrostatic stress is accessed from the hydrostatic pressure in the *Solid Mechanics* module, which is calculated using the Cauchy stress components. The $\sigma_h$ variable can be stored in three different ways: (i) as a model variable, (ii) using an auxiliary variable within a Weak Contribution of the *Solid Mechanics* module or (iii) through an additional PDE. For the concentration-based equation, it has been found that the use of a Weak Contribution reduces inaccuracies in the variable mapping and thus in the gradient calculation. The equivalent plastic strain and its rate are also accessed from the Solid Mechanics module and stored as

model variables. In this case it is not required to store $\varepsilon^p$ as an auxiliary variable or in an additional PDE since $\partial \varepsilon_p / \partial t$ is already calculated internally within the plasticity integration procedure.

Both physics, i.e. displacement and concentration fields, can be solved in a Fully Coupled or Segregated scheme in Comsol Multiphysics. This is discussed in Section 5, even though the couplings are weak since hydrogen concentration does not influence mechanical behaviour in the present work.

## 2.2. Chemical potential-based strategy

The implementation of hydrogen transport modelling with the chemical potential as the dependent variable shows various advantages, as discussed in the Introduction section. To translate the mass balance equation in Eq. (7) to a chemical potential-based problem, the concentration rate $\partial C_L / \partial t$ must be expressed in terms of $\partial \mu_L / \partial t$. The derivation of the following governing equation is detailed in Appendix C. For an isothermal analysis, $T = T_0$, the final governing PDE is:

$$D^* \frac{C_L}{RT_0} \frac{\partial \mu_L}{\partial t} = \nabla \cdot \left( D_L \frac{C_L}{RT_0} \nabla \mu_L \right) - D^* \frac{C_L}{RT_0} \overline{V}_H \frac{\partial \sigma_h}{\partial t} - \theta_T \frac{dN_T}{d\varepsilon_p} \frac{\partial \varepsilon_p}{\partial t} \quad (13)$$

The appearance of the $\sigma_h$ rate in this equation instead of the stress gradient eases hydrogen transport modelling in ABAQUS Explicit, where the determination of hydrostatic stress gradients is more complicated than in ABAQUS Standard, as detailed in Section 3.

### 2.2.1. Comsol multiphysics

The governing Eq. (13) is also implemented through the *Stabilized convection-diffusion* physics in Comsol Multiphysics. In this case, in contrast to the $C_L$-based PDE, the convection term is not present, and the stress influence is governed only by a reaction term.

$$D^* \underbrace{\frac{C_L}{RT_0}}_{d_a} \frac{\partial \mu_L}{\partial t} + \nabla \cdot \left( \underbrace{- D_L \frac{C_L}{RT_0} \nabla \mu_L}_{c} \right) = \underbrace{-D^* \frac{C_L}{RT_0} \overline{V}_H \frac{\partial \sigma_h}{\partial t}}_{f} - \theta_T \frac{dN_T}{d\varepsilon_p} \frac{\partial \varepsilon_p}{\partial t} \quad (14)$$

where, the isotropic diffusion coefficient $c$ includes now $D_L C_L / RT_0$. It has been observed that the determination of $\sigma_h$ rates is not accurate when storing the hydrostatic stress through a Weak Contribution in Comsol Multiphysics and therefore an additional PDE is included where the *absorption coefficient* is equal to one and the source term equal to the mapped variable.

## 3. Implementation in VUMATHT

Heat transfer terms that need to be updated in a VUMATHT are similar to those in a UMATHT, but some peculiarities for the Explicit scheme have to be considered. Previous works on hydrogen transport modelling in ABAQUS Implicit were based on an isoparametric calculation of hydrostatic stress gradients. This procedure requires access to the stress values at neighbouring integration points. However, in the explicit subroutines VUMAT and VUMATHT, ABAQUS passes variables in blocks of material points to enable the vectorized formulation. However, this architecture does not allow the use of utility routines and restricts the access to data at neighbour points, making the stress-gradient calculation practically unfeasible in ABAQUS Explicit. Therefore, the chemical potential-based equation, which only includes rates of $\sigma_h$ and $\varepsilon^p$ as coupling variables, is adopted to be modelled in the VUMATHT.

The verification, 3D analysis and sensitivity study in Sections 5, 6 and 7, respectively, reproduce a bulk material with a uniform initial concentration and a constant equilibrium concentration, both equal to $C_L^0$. However, conditions for initially empty domains or zero-concentration boundary conditions are also detailed in the present framework for the sake of generalisation.

## 3.1. Non-dimensional modelling

To facilitate the scaling of variables and residuals, the hydrogen transport equation is normalised. The following arbitrary choice is made: the reference value $C_L^r$ that normalises $C_L$ is fixed as the initially uniform concentration $C_L^I$ unless this is zero. In that case, $C_L^r$ is fixed as the stress-free concentration in equilibrium with the environment, $C_L^0$:

$$C_L^r = \begin{cases} C_L^I & \text{if } C_L^I > 0 \\ C_L^0 & \text{if } C_L^I = 0 \end{cases} \quad (15)$$

All possible combinations are discussed in Appendix D. Initial and boundary conditions are formally defined as:

$$C_L^I = C_L(\mathbf{x}, t = 0) \quad (16)$$

$$C_L^B = C_L(\mathbf{x} \in \mathscr{S}_H, t) = C_L^0 \exp\left( \frac{\overline{V}_H}{RT} \sigma_h(\mathbf{x} \in \mathscr{S}_H, t) \right) \quad (17)$$

where, $\mathbf{x}$ are the point coordinates and $\mathscr{S}_H$ represents the surface in contact with a hydrogen producing environment. Thus, a Dirichlet boundary condition $C_L^B$ is applied on $\mathscr{S}_H$ boundaries. The derivation of the exponential stress term and the physical meaning of $C_L^0$ are elaborated in Section 3.3. The non-dimensional concentration is then obtained as:

$$\overline{C}_L = C_L / C_L^r \quad (18)$$

Similarly, a chemical potential is defined from $C_L^r$ to scale the governing equations. Substituting $C_L^r$ into Eq. (5) in the absence of stress:

$$\mu_L^r = \mu_L^0 + RT_0 \ln\left( C_L^r / N_L \right) \quad (19)$$

A non-dimensional chemical potential is thus obtained:

$$\overline{\mu}_L = \frac{\mu_L}{\mu_L^r} = \frac{\mu_L^0 + RT_0 \ln(C_L / N_L)}{\mu_L^0 + RT_0 \ln\left( C_L^r / N_L \right)} \quad (20)$$

Since the solved variable is $\overline{\mu}_L$, the expression to evaluate $\overline{C}_L$ is needed within the integration of the governing variable:

$$\overline{C}_L = \frac{N_L}{C_L^r} \exp\left( \frac{\overline{\mu}_L \mu_L^r - \mu_L^0 + \overline{V}_H \sigma_h}{RT_0} \right) \quad (21)$$

It must be taken into account that the step time in ABAQUS Explicit influences the dynamic nature of the problem. Therefore, a trivial step time $\tau_{step} = 1$ is always fixed instead of real time $t$ and diffusivity is scaled accordingly. The artificial lattice diffusion, $D_L^\tau$, represents the square diffusion distance for hydrogen after the real loading time $t_{load}$:

$$D_L^\tau = D_L t_{load} / \tau_{step} \quad (22)$$

For a constant and uniform temperature, Eq. (13) can be rearranged into the following non-dimensional equation:

$$D^* \overline{C}_L \frac{\partial \overline{\mu}_L}{\partial \tau} = \nabla \cdot \left( D_L^\tau \overline{C}_L \nabla \overline{\mu}_L \right) - D^* \overline{C}_L \frac{\overline{V}_H}{\mu_L^r} \frac{\partial \sigma_h}{\partial \tau} - \frac{RT_0}{C_L^r \mu_L^r} \theta_T \frac{dN_T}{d\varepsilon_p} \frac{\partial \varepsilon_p}{\partial \tau} \quad (23)$$

## 3.2. Governing equation and update of variables

The isothermal scaled Eq. (23) is solved through a VUMATHT with the non-dimensional $\overline{\mu}_L$ as the dependent variable and the terms defined by the heat transfer analogy:

$$\underbrace{D^* \overline{C}_L}_{\rho \; \partial U / \partial T} \frac{\partial \overline{\mu}_L}{\partial \tau} = \nabla \cdot \left( \underbrace{D_L^\tau \overline{C}_L \nabla \overline{\mu}_L}_{k_e} \right) - D^* \overline{C}_L \frac{\overline{V}_H}{\mu_L^r} \frac{\partial \sigma_h}{\partial \tau} - \underbrace{\frac{RT_0}{C_L^r \mu_L^r} \theta_T \frac{dN_T}{d\varepsilon_p} \frac{\partial \varepsilon_p}{\partial \tau}}_{r} \quad (24)$$

In this case, the numerical density $\rho$ cannot be not equal to 1 because inertial terms influence mechanical results in ABAQUS Explicit. In the VUMATHT sequence, the internal thermal energy is updated at the end

of the increment, i.e. at $\tau + \Delta\tau$, as:

$$U^{\tau+\Delta\tau} = U^\tau + dU = U^\tau + \frac{\partial U}{\partial T}\left(\overline{\mu}_L^{\tau+\Delta\tau} - \overline{\mu}_L^\tau\right) = U^\tau + \frac{D^*\overline{C}_L}{\rho}\left(\overline{\mu}_L^{\tau+\Delta\tau} - \overline{\mu}_L^\tau\right)$$

(25)

In contrast to the energy update for a UMATHT in ABAQUS Standard, the Krom's term, i.e. the term proportional to the plastic strain rate, is not included but is modelled as a heat source ($r$) that is passed from the VUMAT subroutine. This is detailed in Section 4. The effective conductivity $k_e$ can be extracted from the governing non-dimensional equation and defines the flux vector. Each flux component is calculated and updates the internal variable fluxNew(nblock, $i$):

$$J_L(i) = -D_L^\tau \overline{C}_L \frac{d\overline{\mu}_L}{dx_i}$$

(26)

where, $d\overline{\mu}_L/dx_i$ is accessed at the end of the increment through the internal variable tempgradNew(nblock, $i$). Normalised concentration $\overline{C}_L$, which is an input in Eq. (24), is stored as a state variable and thus it can be accessed at the beginning of the increment as $\overline{C}_L^\tau =$ stateOld. To update this variable, i.e. stateNew $= \overline{C}_L^{\tau+\Delta\tau}$, the relationship with the $\overline{\mu}_L$ value at the end of the increment is used. In addition, the value of $\sigma_h$ at the end of the increment is passed from the VUMAT subroutine.

$$\overline{C}_L^{\tau+\Delta\tau} = \frac{N_L}{C_L^r}\exp\left(\frac{\mu_L^r\overline{\mu}_L^{\tau+\Delta\tau} - \mu_L^0 + \overline{V}_H\sigma_h^{\tau+\Delta\tau}}{RT_0}\right)$$

(27)

Concentration-dependent factors, i.e. $D^*$ and $\theta_T$, also depend on this choice. Following Eq. (8) the operational diffusivity can be expressed only as a function of the dependent variable $\overline{C}_L$ at the end of the increment:

$$D^* = 1 + \frac{K_T N_T^{\tau+\Delta\tau}/N_L}{\left(1 + K_T\overline{C}_L^{\tau+\Delta\tau}C_L^r/N_L\right)^2}$$

(28)

where, density of trapping sites $N_T$ is assumed to be a function of the equivalent plastic strain. Considering the commonly used expression fitted by Kumnick & Johnson (1980) for pure iron [76]:

$$\log N_T^{\tau+\Delta\tau} = 23.26 - 2.55\exp\left(-5.5\varepsilon_p^{\tau+\Delta\tau}\right)$$

(29)

The occupancy in trapping sites, which is included in the Krom's term, can be calculated assuming thermodynamic equilibrium:

$$\theta_T^{\tau+\Delta\tau} = \frac{K_T\overline{C}_L^{\tau+\Delta\tau}C_L^r/N_L}{1 + K_T\overline{C}_L^{\tau+\Delta\tau}C_L^r/N_L}$$

(30)

### 3.3. Boundary and initial conditions

For gaseous hydrogen uptake the boundary chemical potential is determined by a fugacity value $f_{H_2}$ [40,46]:

$$\mu_L^B = \frac{1}{2}\mu_{H_2} = RT_0\ln\left(\sqrt{\frac{f_{H_2}}{p^0}}\right)$$

(31)

where, $p^0$ is a reference pressure. In that case, the boundary concentration can be expressed following an extended Sievert's law:

$$C_L^B = \frac{N_L}{\sqrt{p^0}}\exp\left(\frac{-\mu_L^0}{RT_0}\right)\sqrt{f_{H_2}}\exp\left(\frac{\overline{V}_H\sigma_h^B}{RT_0}\right)$$

(32)

The reference chemical potential in lattice sites $\mu_L^0$ is usually termed as an absorption enthalpy. In the examples assessed in Sections 5–7, the bulk material is assumed in a saturated condition, and thus $C_L^I = C_L^0$. In this situation, the initial and boundary condition for chemical potential-based implementation are simplified: $\overline{\mu}_L^I = 1$ and
$\overline{\mu}_L^B = 1$

However, for simulation of a non-saturated material or for *ex-situ* conditions, i.e. when a zero concentration is fixed at the outer surface, the initial and boundary conditions must be modified accordingly. A procedure to generalise chemical potential-based initial and boundary conditions is detailed in Appendix D.

### 3.4. Increment stability

The maximum time increment $\Delta\tau$ in ABAQUS Explicit is determined by the minimum of the stability limits corresponding to the mechanical response, $\Delta\tau_M$, and to the thermal solution, $\Delta\tau_T$.

$$\Delta\tau \leq \min\{\Delta\tau_M, \Delta\tau_T\}$$

(33)

Following the calibration by Espeseth et al. (2023) [77], correction factors $\xi_M$ and $\xi_T$, that depend on the element type, can be included to account for a conservative approximation. The mechanical stable time depends on the length of the smallest mesh element, $L_{min}$, and on the dilatational wave speed that can be expressed in terms of density, $\rho$, and Lamé parameters $\lambda$ and $\mu$:

$$\Delta\tau_M = \xi_M L_{min}\sqrt{\frac{\rho}{\lambda + 2\mu}}$$

(34)

On the other hand, the stable limit for the heat transfer equation is proportional to $L_{min}^2$ and depends on the effective specific heat transfer, $c_e$, and the effective conductivity $k_e$:

$$\Delta\tau_T = \xi_T L_{min}^2\frac{\rho c_e}{2k_e}$$

(35)

Particularising for the hydrogen transport model, $\rho c_e$ can be substituted by the $\rho\partial U/\partial T$ and $k_e$ terms defined in Eq. (26):

$$\Delta\tau_T = \xi_T L_{min}^2\frac{D^*}{2D_L^\tau}$$

(36)

This density-independent thermal limit means that mass scaling is only effective if the stability is dominated by the mechanical problem, i. e. that $\Delta\tau_M < \Delta\tau_T$. The evolution of $D^*$ during hydrogen diffusion and trap filling or depletion results in a change in the stability limit. Without trapping the operational diffusion approaches one, $D^* \to 1$, but strong retention effects, i.e. high $D^*$ values, increase the stability limit and thus are beneficial to the reduce the computational cost. At the beginning of a simulation with $C_L = C_L^0$ in the smallest element:

$$\Delta\tau_T = \xi_T L_{min}^2\frac{1}{2D_L^\tau}\left(1 + \frac{K_T N_T/N_L}{\left(1 + K_T C_L^0/N_L\right)^2}\right)$$

(37)

Values of $\Delta\tau_T$ and $\Delta\tau_M$ for the verification benchmark and possible mass scaling strategies are assessed in Section 5.2. Additionally, a detailed study of mass scaling and mesh effects is included in Section 7.

## 4. Coupling to VUMAT

Despite the present work focuses on hydrogen transport modelling, the elastoplastic behaviour in ABAQUS Explicit is modelled through a VUMAT to pass an inelastic dissipation contribution as a heat source to the VUMATHT.

### 4.1. Isotropic hardening plasticity

A simple subroutine is considered using an explicit integration of the material constitutive equations. Trial stress components, i.e., $\boldsymbol{\sigma}^{tr}$, are firstly determined using elastic predictors:

$$\boldsymbol{\sigma}^{tr} = \boldsymbol{\sigma}^\tau + 2\mu\boldsymbol{\Delta\varepsilon} + \lambda\,\text{tr}(\boldsymbol{\Delta\varepsilon})\boldsymbol{I}$$

(38)

where, $\boldsymbol{\sigma}$ is the Cauchy stress tensor, $\boldsymbol{\Delta\varepsilon}$ the strain increment tensor, and $\boldsymbol{I}$ the identity tensor. It must be mentioned that the component order storage is different than in ABAQUS Standard. With these stress

components, an equivalent Von Mises stress, $\sigma_e^{tr}$, is calculated and the yielding condition is checked:

$$\sigma_e^{tr} - \sigma_y^\tau > 0 \tag{39}$$

$\sigma_y^\tau$ is the yield stress at the beginning of the increment. A power-law hardening is here assumed as a function of the equivalent plastic strain at the beginning of the increment:

$$\sigma_y^\tau = \sigma_{y0}\left(1 + \frac{E}{\sigma_{y0}}\varepsilon_p^\tau\right)^n \tag{40}$$

where, $\sigma_{y0}$ is the initial yield stress, $n$ the hardening exponent and $E$ the Young's modulus. In the VUMAT, the increment of equivalent plastic strain is not iteratively determined, as in the implicit implementation of a UMAT [78], but it is explicitly obtained in the following form:

$$\Delta\varepsilon_p = \frac{\sigma_e^{tr} - \sigma_y^\tau}{3\mu + \partial\sigma_y/\partial\varepsilon_p} \tag{41}$$

The hardening modulus, $H = \partial\sigma_y/\partial\varepsilon_p$, is derived from the power-law hardening and the determined equivalent plastic strain increment, $\Delta\varepsilon_p$, updates the yield stress:

$$\sigma_y^{\tau+\Delta\tau} = \sigma_y^\tau + \frac{\partial\sigma_y}{\partial\varepsilon_p}\Delta\varepsilon_p \tag{42}$$

Finally, stress components are updated to the value at the end of the increment:

$$\sigma^{\tau+\Delta\tau} = \frac{\sigma'^{tr}}{1 + \frac{3\mu\Delta\varepsilon_p}{\sigma_y^{\tau+\Delta\tau}}} + \lambda tr(\sigma^{tr})I \tag{43}$$

where, $\sigma'^{tr}$ is the deviatoric part of the trial stress tensor. A Jacobian matrix is not required in the explicit algorithm. VUMAT uses Green–Naghdi stress rates, in contrast to most solid elements formulations in ABAQUS. Therefore, significant differences can be observed for large rotations. Bazant & Vorel (2014) [79] demonstrated that this use of Green–Nagdhi stress rates within the VUMAT leads to energy-conservation errors, but the implications for coupled hydrogen transport modelling are out of the scope of the present work.

The update of the specific internal energy is not detailed since it does not affect results, but it is nonetheless updated in the VUMAT for an accurate evaluation of the energy balance. The dissipated inelastic energy, $E_{In}$, is the key term that couples the VUMAT to the hydrogen transport model in the VUMATHT, through a source term. This coupling is activated in ABAQUS when an inelastic heat fraction is included in order to capture heat generation due to plastic straining.

$$E_{In}^{\tau+\Delta\tau} = E_{In}^\tau + \frac{\Delta w_p}{\rho} \tag{44}$$

where, $\Delta w_p$ is the plastic work increment and $E_{In}$ the dissipated inelastic energy per unit mass. Plastic dissipation produces a heat source per unit volume, $r_p$, that is passed to the heat transfer problem:

$$r_p = \eta\frac{\partial w_p}{\partial t} \tag{45}$$

The coefficient $\eta$, between 0 and 1, is included to quantify the fraction of plastic work that is converted into heat [80]. Inversely, the dissipated plastic work might be replaced if the heat source is known, by considering the incremental formulation:

$$E_{In}^{\tau+\Delta\tau} = E_{In}^\tau + r_p\frac{\Delta\tau}{\eta\rho} \tag{46}$$

Zecevic et al. (2020) [16] and Navidtehrani et al. (2021) [81] exploited this coupling between mechanical and heat user-defined behaviours to implement a phase-field model, due to the analogy between the heat transfer equation and the phase field balance. Similarly, the present implementation takes advantage of the similarity between heat transfer and hydrogen diffusion governing equations to define a coupling source term.

### 4.2. Source term

After the stress and strain calculation within the VUMAT code, two state variables must be stored to be used in the VUMATHT, i.e. the hydrostatic stress (SDV1) and the equivalent plastic strain (SDV2). As shown in Fig. 1, the source term in the VUMATHT emerges as an inelastic energy contribution. An *INELASTIC HEAT FRACTION equal to 1 needs to be specified in the material definition to force $\eta = 1$. In that case, the heat source $r$ is defined by the following expression of the $E_{In}$ increment:

$$E_{In}^{\tau+\Delta\tau} = E_{In}^\tau + r\,\frac{\Delta\tau}{\rho} \tag{47}$$

The source term is passed from the VUMAT considering the incremental formulation, i.e. $r\Delta\tau$. The concentration-dependent terms are stored in two state variables (SDV3 and SDV4) as follows:

$$r\Delta\tau = -\underbrace{(D^*\overline{C_L})^\tau\frac{\overline{V}_H}{\mu_L^\tau}}_{SDV3}\left[\sigma_h^{\tau+\Delta\tau} - \sigma_h^\tau\right] - \underbrace{\theta_T^\tau\frac{RT_0}{C_L^\tau\mu_L^\tau}\frac{dN_T}{d\varepsilon_p}}_{SDV4}\left[\varepsilon_p^{\tau+\Delta\tau} - \varepsilon_p^\tau\right] \tag{48}$$

In the ABAQUS Explicit calling sequence, the VUMAT is called before the VUMATHT. Therefore, if SDV3 and SDV4 are stored in the VUMATHT and accessed in the VUMAT to update the dissipated energy, values correspond to the end of the previous increment, i.e. values of $D^*\overline{C_L}$ and $\theta_T$ at time $\tau$. Alternatively, $(D^*\overline{C_L})^{\tau+\Delta\tau}$ and $\theta_T^{\tau+\Delta\tau}$ can be used if SDV3 and SDV4 are directly determined in the VUMAT because $\overline{\mu}_L^{\tau+\Delta\tau}$ is available as tempNew. However, SDV3 and SDV4 storage in the VUMATHT, which is represented by Eq. (66), is simpler and yields the exact same results for the analysed situation.

## 5. Verification for 2D boundary layer

To validate the implementation in ABAQUS Explicit through the proposed VUMATHT + VUMAT scheme, a benchmark problem is simulated: hydrogen transport near a blunting crack tip considering a boundary layer formulation to reproduce small-scale-yielding and plane strain conditions. The geometry and parameters are taken from the classical work of Sofronis & McMeeking (1989) [48], but results including stress-dependent boundary conditions are compared against results obtained by Di Leo & Anand (2013) [40]. This verification also includes the comparison of results with two implicit platforms for hydrogen transport, as detailed in Section 2: ABAQUS Standard and Comsol Multiphysics.

### 5.1. Geometry and parameters

A scheme of the boundary layer geometry that has been modelled is shown in Fig. 2. Only half model is simulated due to symmetry. Following [48], the initial crack tip opening is $b_0 = 10$ μm and the outer radius is $R_b = 0.15$ m. Remote displacements are applied using a VDISP subroutine in ABAQUS Explicit, a DISP subroutine in ABAQUS Standard and a user-defined fixed displacement in Comsol Multiphysics. In ABAQUS Standard, the DISP subroutine is used to defined both the stress-dependent boundary concentration, for the temperature degree of freedom, and the remote displacements. These displacements, $u_x$ and $u_y$, are given by the Linear Elastic Fracture Mechanics (LEFM) theory and are proportional to the stress intensity factor in mode I, $K_I$:

$$u_x = K_I\frac{1+\nu}{E}\sqrt{\frac{R_b}{2\pi}}\cos\left(\frac{\theta}{2}\right)[3 - 4\nu - \cos\theta] \tag{49}$$

**VUMAT for isotropic hardening plasticity**

Update $\sigma_h$ and $\varepsilon_p$ at the end
of an increment:

$\sigma_h \rightarrow$ SDV1
$\varepsilon_p \rightarrow$ SDV2

Update the dissipated
inelastic specific energy:

$$E_{In}^{\tau + \Delta\tau} = E_{In}^{\tau} + r\frac{\Delta\tau}{\rho}$$

**VUMATHT for hydrogen transport**

Balance equation based on the non-dimensional chemical potential

$$D^* \bar{C}_L \frac{\partial \bar{\mu}_L}{\partial \tau} = \nabla \cdot (D_L^{\tau} \bar{C}_L \nabla \bar{\mu}_L) + r$$

SDV3          SDV4
  ↑            ↑

A heat source
is passed to the
VUMATHT

$$r = -D^* \bar{C}_L \frac{\bar{V}_H}{\mu_L^r} \frac{\partial \sigma_h}{\partial \tau} - \frac{RT_0}{C_L^r \mu_L^r} \theta_T \frac{dN_T}{d\varepsilon_p} \frac{\partial \varepsilon_p}{\partial \tau}$$

**Fig. 1.** *Flowchart of VUMAT and VUMATHT subroutines.* The strategy to optimize the implementation of stress-assisted hydrogen diffusion and trapping depending on plastic strain is to pass a heat source from the VUMAT to the VUMATHT as a function of $\sigma_h$ and $\varepsilon_p$ rates. This heat source is defined in the VUMAT through the dissipated inelastic specific energy. The variables $\sigma_h$ and $\varepsilon_p$ are stored solution dependent variables (SDVs).
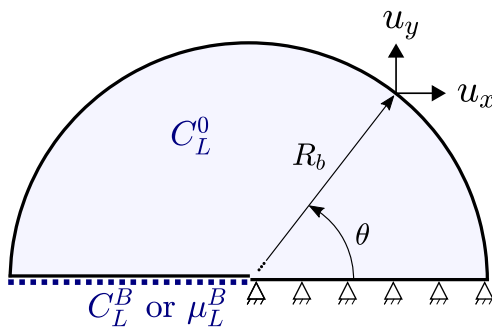


**Fig. 2.** *Scheme of boundary layer model with remote displacements to reproduce small scale yielding conditions.* The bulk is initially with a lattice concentration $C_L^0$ and the boundary conditions are $C_L^B = C_L^0 \exp(\sigma_h \bar{V}_H / RT)$, for the concentration-based approach or $\mu_L^B$ for the chemical potential governing equation.

$$u_y = K_I \frac{1+\nu}{E} \sqrt{\frac{R_b}{2\pi}} \sin\left(\frac{\theta}{2}\right) [3 - 4\nu - \cos\theta] \qquad (50)$$

where, $\nu$ is the Poisson's coefficient and $\theta$ the angle with the symmetry plane, as depicted in Fig. 2. Loading $K_I$ increases linearly with time until the maximum equal to 89.2 MPa$\sqrt{m}$ is reached at $t_{load}$ [54].

The mesh consists of 1308 elements for both ABAQUS Standard and Explicit results. Thus, the mesh is finer than in classical works [48,54] but coarser in comparison to Di Leo & Anand (2013) [40]. However, a biased mesh is considered and thus the element size at the crack tip is approximately $b_0/20$.

The element type for each implementation is shown in Table 3. It must be noted that CPE8RT are biquadratic displacement but bilinear temperature elements. In contrast, linear quad elements (CPE4RT) are

**Table 3**
*Element type and discretization for the implementation frameworks that are evaluated.* A higher discretization order in Comsol Multiphysics is needed to avoid spurious hydrostatic stress near the deformed crack tip. Linear discretization is possible in ABAQUS due to the selective reduce integration that prevents volumetric locking.

| | Concentration balance ($C_L$) | Chemical potential balance ($\mu_L$) |
|---|---|---|
| ABAQUS user-defined subroutines | Quad element with biquadratic displacement and bilinear temperature. Reduced integration and plane strain. CPE8RT | Quad element with bilinear displacement and temperature. Reduced integration and plane strain. CPE4RT |
| Comsol Multiphysics PDEs | Quad element with cubic displacement and quadratic concentration. Full integration and plane strain. | Quad element with cubic displacement and quadratic chemical potential. Full integration and plane strain. |

used in ABAQUS Explicit because 8-node elements are not available in 2D. For elements in Comsol Multiphysics there is not any nomenclature, but the discretization can be defined for each individual *Physics*. In contrast to ABAQUS elements, that use a selective reduce integration method to prevent volumetric locking, a cubic order discretization of the displacement field has been required to avoid spurious hydrostatic stresses in Comsol Multiphysics due to the extremely high plastic deformation at the crack tip. The use of linear or quadratic elements in Comsol is also possible if a mixed formulation for nearly incompressible materials is activated.

Parameters for the mechanical response and for hydrogen transport are extracted from Sofronis & McMeeking (1989) and are collected in Table 4. Assuming a $\mu_L^0$ value of 28.6 kJ/mol [40], the reference concentration $C_L^r = C_L^I = C_L^0 = 2.084 \times 10^{21}$ atoms/m$^3$ corresponds to a chemical potential $\mu_L^r = -19.576$ kJ/mol. The density of trapping sites $N_T$ is modelled through Eq. (29).

*5.2. Results for ABAQUS Explicit*

Distributions of nodal temperatures in ABAQUS Explicit are plotted in Fig. 3 to assess the non-dimensional chemical potential, $\bar{\mu}_L$, considering two different loading times: $t_{load} = 1.3$ and $130$ s. The range of loading times mimic the original references [40,48,54] in order to evaluate transient effects and the influence of the trap creation rate. The normalised concentration, $C_L/C_L^0$, is also plotted.

For a slow loading, i.e. for 130 s, the $\bar{\mu}_L$ peak appears at a higher distance from the crack tip. However, since $\mu_L^r < 0$, the peak represents a minimum in $\mu_L$ due to the combination of hydrostatic stress and low $C_L$ values. Nevertheless, the $C_L$ maximum is located near the crack tip when the hydrostatic stress maximum is found.

On the other hand, the fast load, i.e. $t_{load} = 1.3$ s, results in a strong sink due to the rapid plastic deformation increase (high $\partial\varepsilon_p/\partial t$ values), that produces a reduction in $\mu_L$ near the deformed crack tip. However, the peak of $\bar{\mu}_L$ is not observed at the crack surface because its value is fixed to the boundary value, i.e. $\bar{\mu}_L^B = 1$. This maximum in $\bar{\mu}_L$, or minimum in $\mu_L$, is manifested as a low hydrogen concentration $C_L$. As originally observed by Krom et al. (1999) [54], the fast trap creation may result in the depletion of lattice sites. This effect is also observed in Fig. 3b.
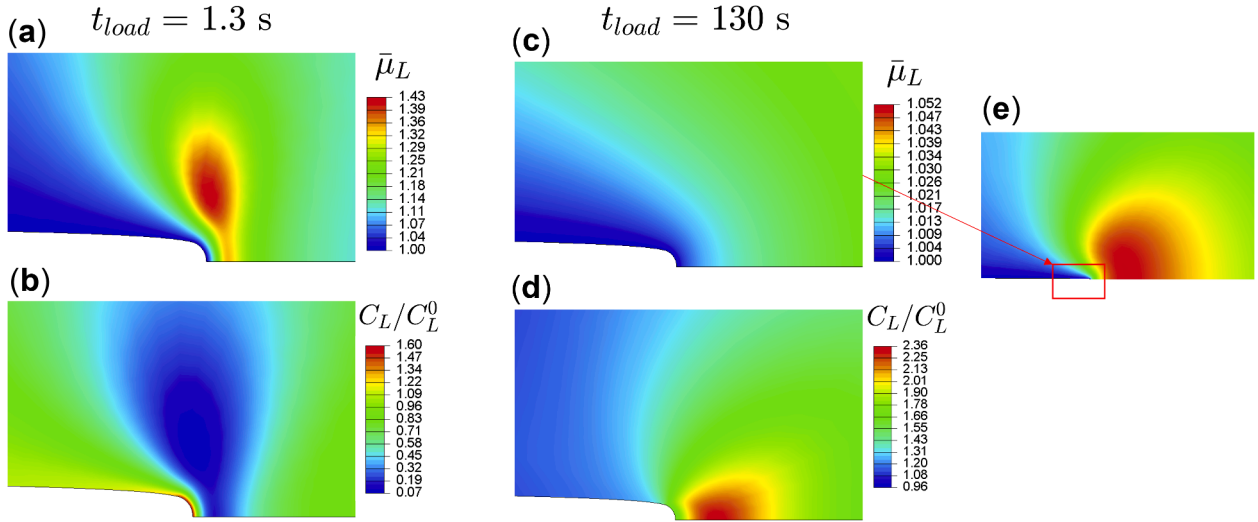
For results shown in Fig. 3, a numerical density $\rho$ equal to $10^{-4}$ was fixed. However, as previously mentioned, the stability limit and the

**Table 4**
Elastoplastic and diffusion parameters for the verification problem [48].

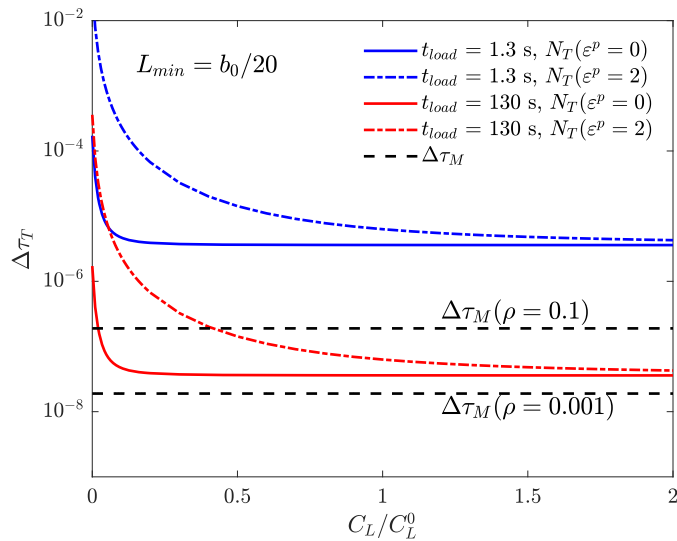| E (GPa) | $\nu$ | $\sigma_{y0}$ (MPa) | n | $T_0$ (K) |
|---|---|---|---|---|
| 207 | 0.3 | 250 | 0.2 | 300 |
| $D_L$ (m$^2$/s) | $\bar{V}_H$(m$^3$/mol) | $N_L$ (sites/m$^3$) | $C_L^0$(atoms/m$^3$) | $E_B$ (kJ/mol) |
| $1.27 \times 10^{-8}$ | $2.0 \times 10^{-6}$ | $5.1 \times 10^{29}$ | $2.084 \times 10^{21}$ | 60 |

**Fig. 3.** *Normalised chemical potential and hydrogen distribution in lattice sites.* Results are obtained through the proposed combination VUMATHT + VUMAT in ABAQUS Explicit for two different loading times. (a) normalised chemical potential for 1.3 s; (b) normalised concentration for 1.3 s; (c) normalised chemical potential for 130 s; and (d) normalised concentration for 130 s. The maximum of $\bar{\mu}_L$ for 130 s is located far from the crack tip, as shown in the larger region in (e).

accuracy of results depend on this choice. For the present problem and the original parameters from Sofronis & McMeeking (1989) [48] (Table 4), the $\Delta\tau_T$ value can be determined at the beginning of the simulation, i.e. for $\tau = 0$. It must be noted that, since the simulation time is scaled, $D_L^\tau = D_L t_{load}/\tau_{step}$, the increments are also non-dimensional.

$$\Delta\tau_T = \xi_T L_{min}^2 \frac{1}{2D_L t_{load}} \left(1 + \frac{K_T N_T/N_L}{(1 + K_T C_L/N_L)^2}\right) \qquad (51)$$

The smallest element in the mesh that is chosen for the present validation has an approximate length of $L_{min} = b_0/20$, where $b_0$ is the initial crack tip opening equal to 10 µm. Since the smallest element is placed at the crack tip, plastic deformation and the consequent increase in trap density should be assumed. Stability limit values for the thermal problem are plotted in Fig. 4 considering parameters from Table 4 and the extreme loading times, 1.3 and 130 s, respectively. The

concentration dependence is governed by $D^*$: trapping effects are more pronounced at lower concentrations and almost negligible for the saturated regime. On the other hand, the stability limits for the mechanical problem, $\Delta\tau_M$, considering two numerical density values are plotted for the sake of comparison. It can be observed that the thermal problem only governs the time increment minimum for a high numerical density or for a long step time.

A quasi-static problem is here simulated and thus the choice of the numerical density $\rho$ is limited. High $\rho$ values reduce the number of required increments but introduce undesired inertial effects. To discard inertial effects in the present results, the evolution of the nodal temperature value, i.e. $\bar{\mu}_L$, is plotted at $x/b = 1$ in Fig. 5a, where $x$ is the distance from the crack tip and $b = 4.7b_0$ the final crack tip opening. Due to the sink effect, $\bar{\mu}_L$ increases but a substantial numerical noise is obtained for $\rho = 10^{-3}$, both for $t_{load} = 1.3$ s and 3.25 s. For longer loading times the noise is also present, but to a lesser extent because the evolution of $\bar{\mu}_L$ is smoother at the end of the increment when plastic deformation is large. In the detail of this evolution showed in Fig. 5b it can be concluded that a value of $\rho = 10^{-4}$ is low enough to avoid inertial effects and a mesh refinement does not change results. Nevertheless, the stable time increment for this very low $\rho$ value is governed by the mechanical stability condition and $\Delta\tau < 10^{-8}$ is needed for the considered fine mesh, resulting in extremely high computational times. Therefore, the feasibility of crack tip simulations is limited using the present approach and only presented here for benchmarking purposes. On the contrary, the mesh size and mass scaling required for notches results in practical computation times, as detailed in Sections 6 and 7.

In the absence of strong gradients, hydrogen transport problems do not usually suffer from convergence issues and therefore the efficiency of implicit schemes is superior to the present explicit implementation. However, explicit schemes are computationally advantageous for some damage models with slow convergence. The aim of the proposed strategy is thus to inform these damage models in a coupled explicit scheme.



**Fig. 4.** *Stability limits for the thermal problem as a function of hydrogen concentration in the Explicit scheme.* Limits for the mechanical problem are plotted for two numerical density values to determine whether the stable increment size is governed by the mechanical ($\Delta\tau_T > \Delta\tau_M$) or by the diffusion ($\Delta\tau_T < \Delta\tau_M$) problem. The diffusion-controlled stability only occurs for high densities, e.g. $\rho = 0.1$, and high concentrations where trapping effects are weaker.

### 5.3. Validation

Once the stable time sensitivity has been assessed for the implementation in ABAQUS Explicit, distributions of hydrogen concentration along the crack plane are compared against the other implicit implementation strategies. Following the same loading time values simulated by Krom et al. (1999) [54], results are shown for $t_{load} = 1.3$, 3.25, 13 and 130 s. It is important to consider that distributions of lattice
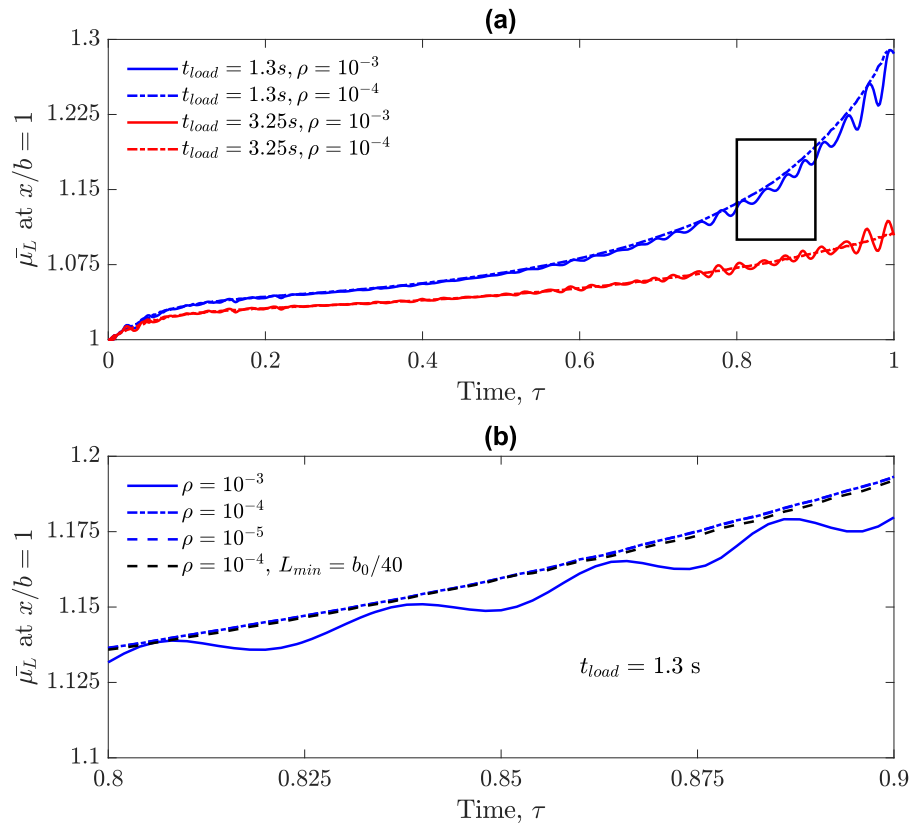
**Fig. 5.** *Influence of mass scaling on the evolution of non-dimensional chemical potential.* The $\bar{\mu}_L$ value is plotted at a distance to the crack tip equal to the final crack tip opening, $x = b$. In (a) two different loading times (1.3 and 3.25 s) and two numerical densities are compared, showing numerical oscillations due to dynamic effects for $\rho = 10^{-3}$ but a smooth evolution for $\rho = 10^{-4}$. A detail of the $\bar{\mu}_L$ evolution is plotted in (b) for a loading time of 1.3 s. A lower density, i.e. $\rho = 10^{-5}$, or a smaller element size, i.e. $L_{min} = b_0/40$, produce very similar results demonstrating the mesh and mass scaling convergence.

concentration are sensitive to the chosen mechanical and hydrogen-related parameters. For instance, higher concentrations would be obtained for a material with a higher yield stress due to the hydrostatic stress level [82]. Similarly, diffusion and trapping parameters determine the transient accumulation and therefore the dependency of $C_L$ distributions on the loading time [56,72,83].

Fig. 6a compares the normalised $C_L$ distributions obtained in ABA-QUS Explicit, using the combination VUMAT+VUMATHT detailed in Sections 3 and 4, to results from ABAQUS Standard, where a UMATHT has been used. Hydrostatic stress and equivalent plastic strain were accessed and stored in a USDFLD subroutine for ABAQUS Standard. The agreement is satisfactory, especially for $t_{load} = 130$ s.

Similarly, results for ABAQUS Explicit are validated against those from the implementation in Comsol Multiphysics considering the concentration-based governing equation (Section 2.1.2). In that case, an implicit scheme, a Backward differentiation formula (BDF) is used as a time-dependent solver. This comparison is shown in Fig. 6b and corresponds to a segregated step approach. Results agree for all the loading times, but a slight deviation is found for $t_{load} = 130$ s, in contrast to the comparison with ABAQUS Standard. However, when the chemical potential-based equation is solved, results between Comsol Multiphysics and ABAQUS Explicit perfectly agree for all the loading rates (Fig. 6c). This indicates that the choice of the solution variable may influence slightly the obtained results, probably due to the determination of concentration-dependent terms and of the $\sigma_h$. In addition, differences in time integration schemes are expected to affect the rate terms in the chemical potential-based PDE whereas the hydrostatic stress gradient calculation procedure influence results in the concentration-based approach. Contours of $\mu_L$ and $C_L/C_L^0$ are also plotted in Fig. 7 for the chemical potential-based implementation in Comsol Multiphysics to

demonstrate that the prediction of hydrogen redistribution agrees with ABAQUS Explicit (Fig. 3).

Results obtained using the combination VUMAT + VUMATHT are also compared with distributions from Di Leo & Anand (2013) [40] because that work inspired the present strategy based on the chemical potential and these authors also assessed different loading times. As shown in Fig. 6d, the influence of loading rate shows similar trends, but the deviations are substantial and were firstly attributed to differences in meshing or to the solution schemes. However, mesh sensitivity studies have been carried out using the implicit models in ABAQUS Standard and Comsol Multiphysics, finding a convergence of results to the distributions shown in Fig. 6a–c. Similarly, smaller time increments and tighter tolerances have not produced significant differences. Moreover, Comsol Multiphysics results have been obtained for both segregated and fully coupled schemes, yielding the same results. On the other hand, hydrostatic stress and equivalent plastic strain (Fig. 8) distributions are compared, and substantial differences are not found. Only for the $\varepsilon_p$ value at the crack tip for ABAQUS Explicit a deviation is observed, which is attributed to the linear discretization of the elements.

For $t_{load} = 1.3$ s, Krom et al. (1999) [54] found a total depletion of lattice sites, i.e. $C_L = 0$, at $x/b = 0.6$–0.7, approximately, due to the fast creation of traps but without considering the hydrostatic stress influence on the boundary condition. Di Leo & Anand (2013) [40] found a larger depleted zone when stress-dependent boundary conditions were included and attributed this result to a "higher demand" for lattice hydrogen. It is true that the surface $C_L$ value is higher when the hydrostatic stress is accounted for, and this results in a higher $\theta_T$ that enhances Krom's term and the depletion of lattice sites. However, the higher $C_L$ surface value also represents a greater hydrogen source and might compensate lattice depletion, as it is found in the present work. Even though these deviations are still not totally explained, results of the
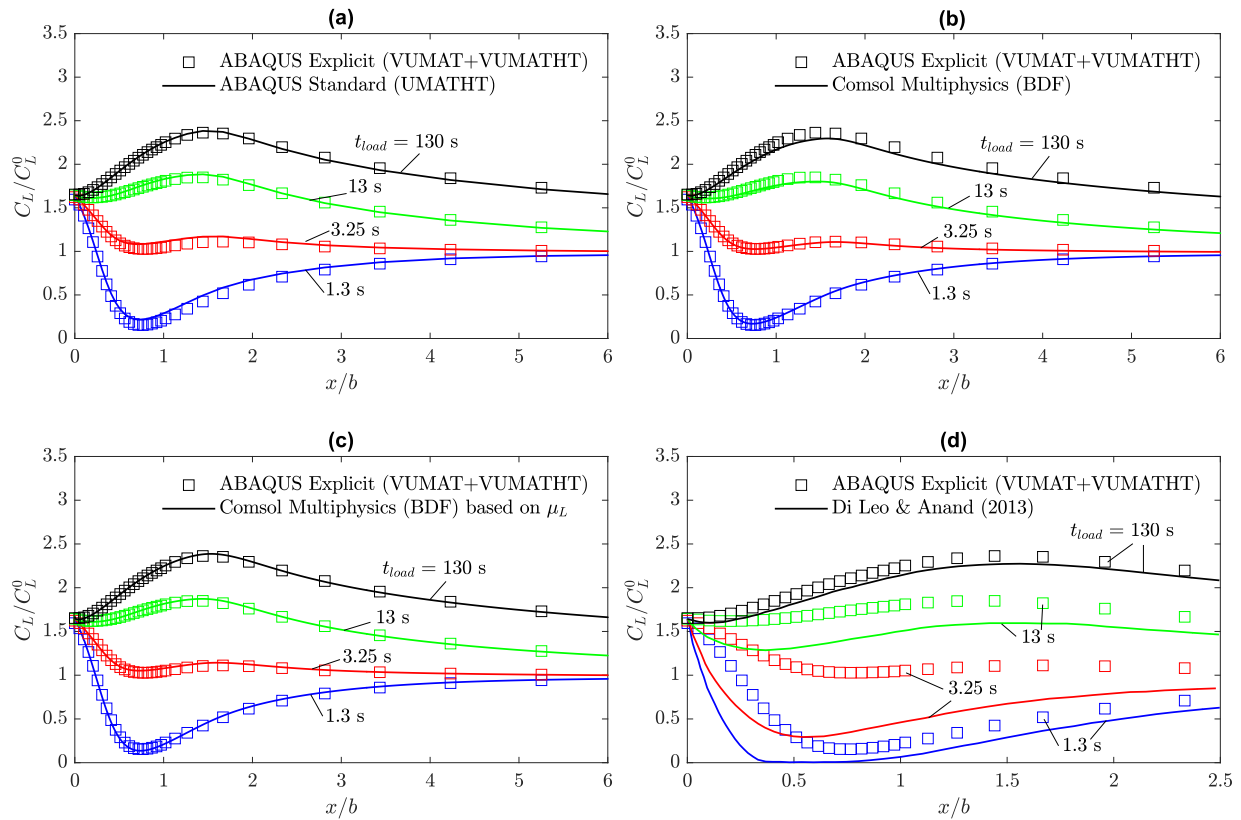
**Fig. 6.** *Distribution of normalised hydrogen concentration in lattice sites for different loading times.* Comparison between results from the proposed implementation in ABAQUS Explicit and: (a) results from ABAQUS Standard, (b) results from Comsol Multiphysics with an implicit solver (BDF) and a PDE based on concentration or (c) based on the chemical potential, and (d) results obtained by Di Leo & Anand (2013) [40].
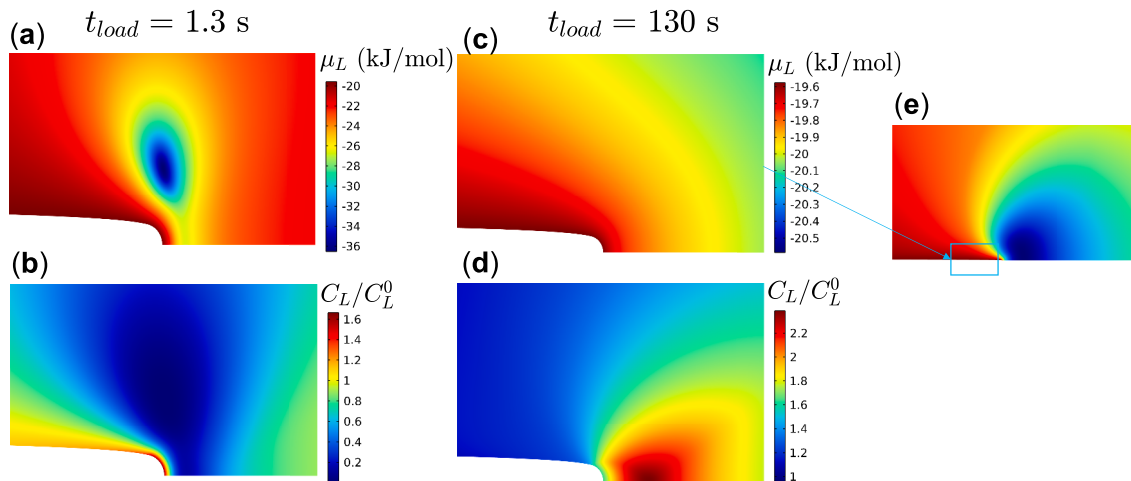


**Fig. 7.** *Normalised chemical potential and hydrogen distribution in lattice sites.* These results correspond to the chemical potential-based implementation in Comsol Multiphysic for two different loading times. (a) chemical potential for 1.3 s; (b) normalised concentration for 1.3 s; (c) chemical potential for 130 s; and (d) normalised concentration for 130 s. The minimum of $\mu_L$ for 130 s is located far from the crack tip, as shown in the larger region in (e).

present model perfectly agree with those from Di Leo & Anand (2013) [40] if the crack surface is assumed to be insulated, as shown in Fig. 9. Therefore, deviations in Fig. 6d must be caused by differences in the determination of hydrostatic stress or plastic strain rates when a constant chemical potential is fixed as a boundary condition. Different time integration schemes are likely to influence these rates and thus the $C_L$ distributions. Deviations can also be caused by the near incompressible behaviour for elements under high plastic deformations. In this case, even if the $\sigma_h$ distributions agree, the gradient or rate determination can

be affected by spurious noise.

## 6. Case study for 3D modelling

One of the advantages of the VUMAT + VUMATHT implementation of hydrogen transport based on the chemical potential variable is that hydrostatic stress gradients are not required and the extension to 3D modelling is straightforward. Modifications in the subroutine coding are not needed because of the rate-based formulation. The capabilities of
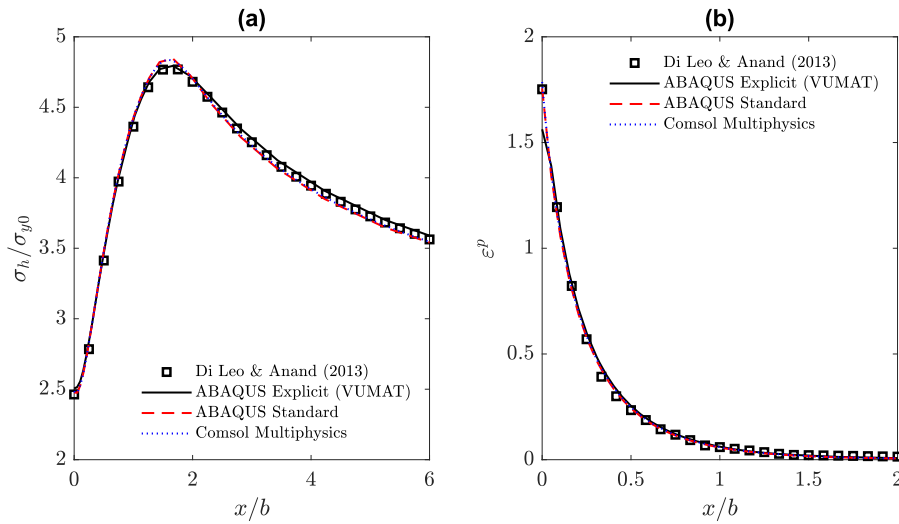
**Fig. 8.** *Comparison between results using different schemes and results from Di Leo & Anand (2013)* [40]. Distribution of (a) normalised hydrostatic stress and (b) equivalent plastic strain along the crack tip plane.
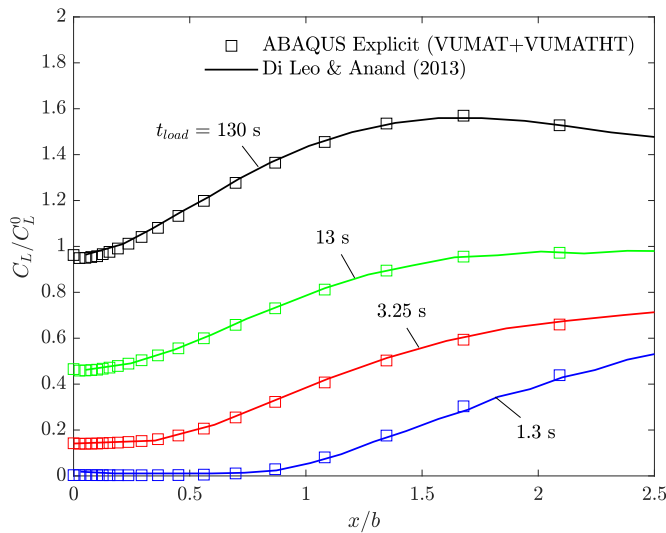


**Fig. 9.** *Distribution of normalised hydrogen concentration in lattice sites for different loading times and an insulated crack surface.* Validation of the proposed implementation in ABAQUS Explicit in comparison to results obtained by Di Leo & Anand (2013) [40] for an insulated case.



**Fig. 10.** *Round notched specimen from ASTM G142-98(2022).* (a) Section view with dimensions in mm and (b) 3D view of the simulated quarter of the specimen.

this framework are assessed for a 3D round tensile specimen with a V-notch. Dimensions are selected for the sample standardised in ASTM G142-98(2022) for the determination of susceptibility of metals to hydrogen embrittlement (Fig. 10). Only a quarter of the model is simulated, and the corresponding symmetry conditions are imposed.

A constant $\bar{\mu}_L = 1$ is imposed to the outer surfaces and as initial value, which reproduces a boundary at equilibrium with $C_L^0$ and the same initial concentration. These values and all the hydrogen-related and mechanical parameters are the same than for the previous verification (Table 4). Mechanical loading is performed through a rising axial displacement, $u_y$, that reaches a value of 0.2 mm at the end of the loading time, which is here considered as $t_{load} = 300$ s. The numerical density is fixed to $\rho = 10^{-3}$ to reduce the computation time, and three different element types are evaluated: (i) linear hexahedrons (C3D8T), (ii) linear tetrahedrons (C3D4T) and (iii) second-order modified tetrahedrons with hourglass control (C3D10MT). Despite the element size is similar in all cases, the number of elements increases for a tetrahedron-based mesh. Similarly, the second-order tetrahedron produces a higher
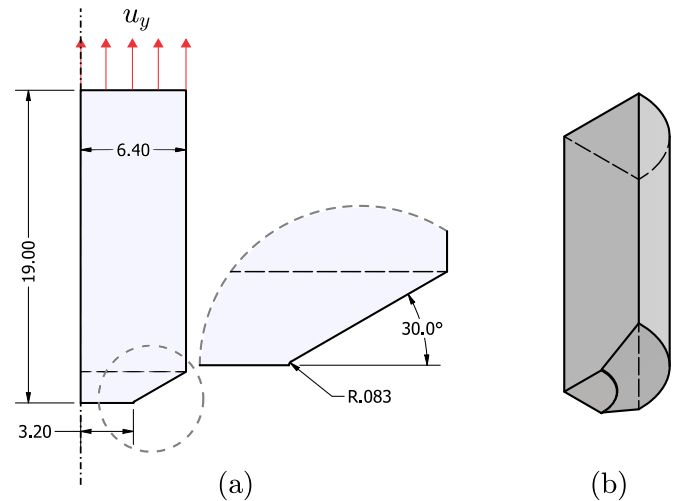
**Table 5**

Description of different meshes and the corresponding CPU time and stability parameters.

| Element type | Elements | Nodes | CPU time (s) | at $\tau = 1$ $\Delta\tau$ | Kinetic Energy | Total Energy |
|---|---|---|---|---|---|---|
| C3D8T | 38,766 | 42,140 | 495,008 | $4.18 \times 10^{-6}$ | 0.094953 | 584.1 |
| C3D4T | 60,175 | 12,459 | 74,845 | $5.75 \times 10^{-6}$ | 0.13630 | 585.3 |
| C3D4T ($0.1\rho$) | 60,175 | 12,459 | 226,518 | $1.84 \times 10^{-6}$ | 0.01281 | 585.3 |
| C3D10MT | 60,175 | 90,109 | $1.11 \times 10^{6}$ | $8.13 \times 10^{-7}$ | 0.114492 | 585.3 |

number of nodes. Therefore, despite the stable increment slightly changes the CPU time strongly depends on the element choice, as shown in Table 5 at the end of the increment, i.e. at $t = t_{load}$ or $\tau = 1$.

The C3D4T presents the best stable limit because $\Delta\tau$ is slightly higher and the minimum number of nodes (12,459). However, a strong numerical noise is observed in highly deformed regions near the crack tip. Spurious stresses for the linear tetrahedrons result in a noisy $\bar{\mu}_L$ solution, and hence in unstable $C_L/C_L^0$ distributions, as shown in Fig. 11. The kinetic energy is higher than for the hexahedrons, but still low in comparison with total energy (Table 5) and thus inertial effects are not the cause of the noise. Additionally, a decrease in the numerical density by a factor of 10, i.e. $0.1\rho$, reduces the kinetic energy but does not prevent numerical instabilities for C3D4T elements, as shown in Fig. 11. Therefore, it can be concluded that spurious $\bar{\mu}_L$ and $C_L$ distributions for C3D4T elements are caused by volumetric locking and not by inertial effects. In contrast to the linear hexahedrons, and also to the linear quads analysed in Section 5 (CPE4RT), volumetric locking is not prevented in C3D4T. For this reason, linear tetrahedrons are not recommended for plastic deformation simulations [84].

As an alternative, the use of second-order tetrahedrons with a modified formulation (C3D10MT) avoids the numerical instabilities and gives similar results than the C3D8T. However, the stable time increment is lower and the number of nodes higher, resulting in an excessive computational cost.

## 7. Sensitivity to mass scaling and mesh size

The notched tensile test conditions from Section 6 are reproduced here but considering a 2D axisymmetric model in order to assess the influence of numerical density, i.e. mass scaling, and mesh size in

reasonable computational times. Loading and material parameters are also the same. The elements used for this study are quadrilateral axisymmetric elements with reduced integration and temperature degree of freedom (CAX4RT). Biased mesh is considered with the $L_{min}$ defined by smallest element characteristic length, which is located at the crack tip, as shown in Fig. 12 for $L_{min} = 0.01$ mm, approximately 8 times smaller than the notch radius.

A higher number of nodes is obtained due to a mesh refinement from 0.04 to 0.01 mm, as observed in Table 6. However, the increase is moderate due to the biased mesh strategy. The higher CPU time for the finer mesh is caused by the stability condition, i.e. by $\Delta\tau$ increments. The influence of mass scaling is also assessed in this example for three different values: $10^{-4}$, $10^{-3}$ and $10^{-2}$. The lower $\rho$ value, i.e. $10^{-4}$, captures quasi-static conditions as demonstrated by the low kinetic energy computed (Table 6) at the expense of smaller stable increments and longer computation times.

Stable non-dimensional time increments, $\Delta\tau$, are plotted in Fig. 13 against $\rho^{0.5}$ and $L_{min}$ with the aim of evaluating the dominance of mechanical or thermal stability. Fig. 13a shows a surface fitted to an expression $\Delta\tau_1 = m_1\rho^{0.5}L_{min}$, which corresponds to the mechanical stability condition (Eq. (34)). The linear slope in the $\Delta\tau$-$L_{min}$ plane fits the low-density region ($\rho = 10^{-4}$) but does not match the high-density results ($\rho = 10^{-2}$). On the contrary, the surface $\Delta\tau_1 = m_1\rho L_{min}^2$, shown in Fig. 13b, follows the thermal stability condition (Eq. (35)) and fits only the high-density points ($\rho = 10^{-2}$). For a problem totally controlled by the thermal-diffusion equations, $\Delta\tau$ should be independent of $\rho$ (Eq. (37)). These results indicate that the problem is dominated by the mechanical stability for low $\rho$ values but approaches the thermal-diffusion condition for high numerical densities, confirming the preliminary stability analysis from Section 5.
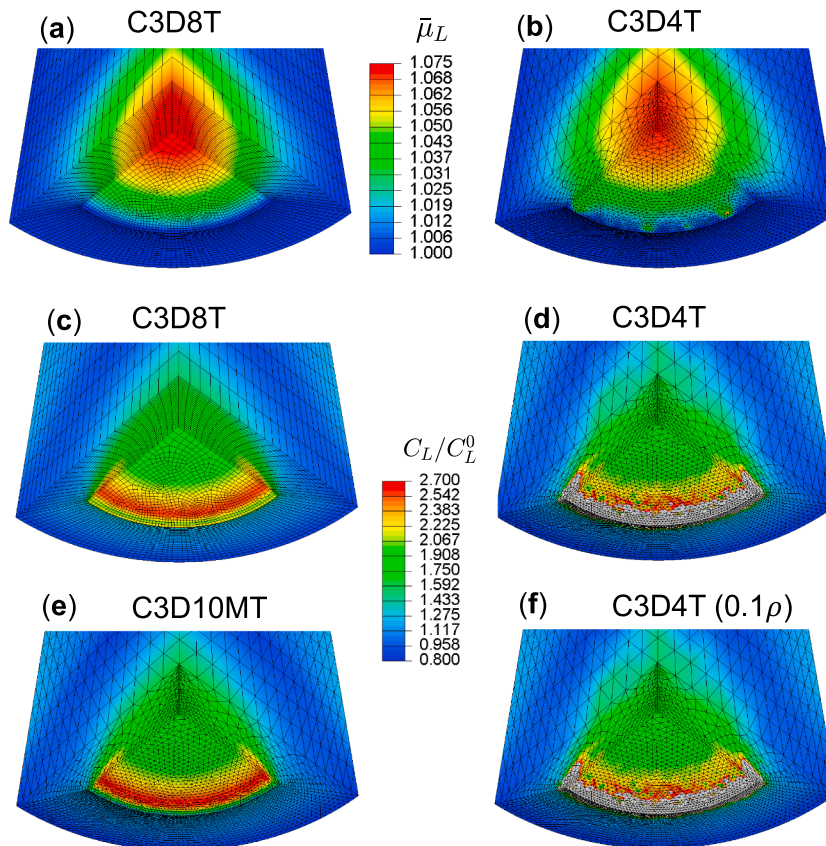


**Fig. 11.** *Comparison of results for different types of 3D elements.* Normalised chemical potential is plotted in (a) for linear hexahedrons (C3D8T) and in (b) for linear tetrahedrons (C3D4T). Normalised hydrogen concentration is plotted in (c) for linear hexahedrons (C3D8T), in (d) for linear tetrahedrons (C3D4T) and in (e) for second-order tetrahedrons with a modified formulation (C3D10MT). Results for C3D4T are spurious even if the density is reduced to $0.1\rho$ (f).
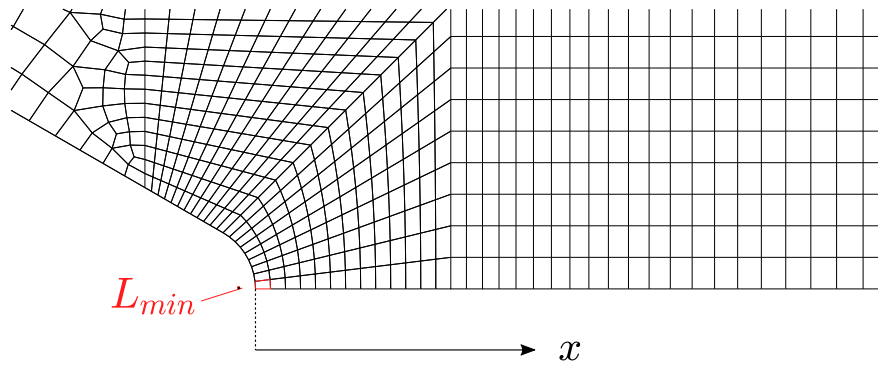
**Fig. 12.** *Mesh for $L_{min} = 0.01$ mm in the axisymmetric model.* The element size that determines the stable time increment corresponds to the smallest element at the crack tip. The $x$ coordinate is graphically defined to plot results in the notch plane.

**Table 6**
Influence of mesh size and numerical density on the CPU time, stable time increment and kinetic energy.

| Minimum element size, $L_{min}$ (mm) | Numerical density, $\rho$ | Nodes | CPU time (s) | at $\tau = 1$ $\Delta\tau$ | Kinetic Energy | Total Energy |
|---|---|---|---|---|---|---|
| | $10^{-4}$ | | 112,928 | $1.04 \times 10^{-7}$ | 0.00487 | 2341.32 |
| 0.01 | $10^{-3}$ | 3128 | 33,226 | $3.86 \times 10^{-7}$ | 0.04914 | 2341.32 |
| | $10^{-2}$ | | 10,672 | $1.27 \times 10^{-6}$ | 0.46584 | 2341.33 |
| | $10^{-4}$ | | 33,229 | $3.25 \times 10^{-7}$ | 0.00449 | 2341.32 |
| 0.02 | $10^{-3}$ | 2310 | 10,396 | $1.07 \times 10^{-6}$ | 0.05041 | 2341.32 |
| | $10^{-2}$ | | 3327 | $3.37 \times 10^{-6}$ | 0.45757 | 2341.33 |
| | $10^{-4}$ | | 21,907 | $3.98 \times 10^{-7}$ | 0.00458 | 2341.33 |
| 0.04 | $10^{-3}$ | 2048 | 7067 | $1.20 \times 10^{-6}$ | 0.05141 | 2341.33 |
| | $10^{-2}$ | | 2237 | $3.76 \times 10^{-6}$ | 0.44290 | 2341.33 |

Sensitivity of results to the mesh size is analysed in Fig. 14a and b. Distributions of normalised hydrogen concentration in lattice sites, $C_L/C_L^0$, are not captured by the coarser mesh near the surface and at the maximum, which is located at the hydrostatic stress peak for the simulated loading time ($t_{load} = 300$ s). However, the convergence of results after mesh refining is demonstrated for $L_{min} = 0.01$ mm. The required element size for mesh convergence is expected to depend on the notch or crack radius and thus on the triaxiality. Comparing Fig. 14a and b it can be concluded that mesh influence does not depend on the choice of $\rho$. It is interesting to note that $C_L/C_L^0$ distributions for $L_{min} = 0.01$ mm at the end of the increment (Fig. 14c) are not affected by the numerical density value despite the numerical oscillations observed for $\rho = 10^{-2}$ at the beginning of the increment. This noise is plotted in Fig. 14d for the evolution of the dependent variable, $\overline{\mu}_L$, at approximately $x = R_{notch}/2$. It is observed that the oscillations are damped after $\tau = 0.2$ and thus results at the end of the increment ($\tau = 1$) are not affected by mass scaling. This finding contrasts with the amplified oscillations obtained for the crack tip conditions simulated in Section 5. Differences are attributed to the

higher stress and strain state for the crack tip.

## 8. Conclusions

A hydrogen transport model has been presented including stress-assisted diffusion, trapping effects and physically based uptake. Despite numerous works have previously implemented this transport model in commercial finite element software, there is an absence of implementation strategies for explicit schemes. This research gap is hindering the extension of available explicit codes modelling damage to hydrogen embrittlement predictive tools.

Limitations were detected for the extension of hydrogen transport implicit codes to ABAQUS Explicit. Access to neighbour points is unpractical in Explicit subroutines due and therefore makes unfeasible the determination of hydrostatic stress gradients. To circumvent these limitations, a chemical potential-based formulation has been implemented in a user-defined subroutine (VUMATHT) that exploits the analogy between heat transfer and hydrogen transport. A source term that depends on the hydrostatic stress and equivalent plastic strain rates is implemented and captures mechanical effects on hydrogen redistribution near a crack tip at different loading rates. The use of chemical potential as the dependent variable to solve the transport problem has been inspired by the work of Di Leo & Anand (2013) [40] and the heat transfer analogy follows a previous work, Díaz et al. (2016) [41] focused on ABAQUS Standard subroutines.

Explicit schemes for hydrogen transport near a crack are not optimal since the mesh is particularly refined and the smallest element, i.e. near the crack tip, results in an extremely low stability limit and thus in excessive computation times. Nevertheless, the benchmark problem from Sofronis & McMeeking (1989) [48], Krom et al. (1999) [54] and Di Leo & Anand (2013) [40] has been used to validate results and compare different implementation strategies. Different loading times have been simulated and the depletion of lattice sits due to the fast creation of traps has been captured, as in previous works [54]. In addition, the stress-dependent hydrogen concentration on the crack surface is reproduced naturally by the constant chemical potential boundary condition. Despite deviations are found in comparison to Di Leo & Anand (2013) [40], the results obtained in ABAQUS Explicit show a perfect agreement with concentration-based formulations in ABAQUS Standard and with both concentration and chemical potential-based frameworks in Comsol Multiphysics. Convergence of results for sufficiently fine meshes and low numerical densities in the Explicit scheme is demonstrated. Quasi-static conditions are reproduced, and mass scaling is limited to numerical densities below $10^{-3}$ to avoid oscillations due to inertial effects.

The influence of mesh and mass scaling on the explicit problem stability has also been addressed. Hydrogen transport is solved through a heat transfer analogy and thus a thermal stability condition can be defined. It is concluded that the stable time increment is determined by the mechanical stability condition for low density values. Only for an
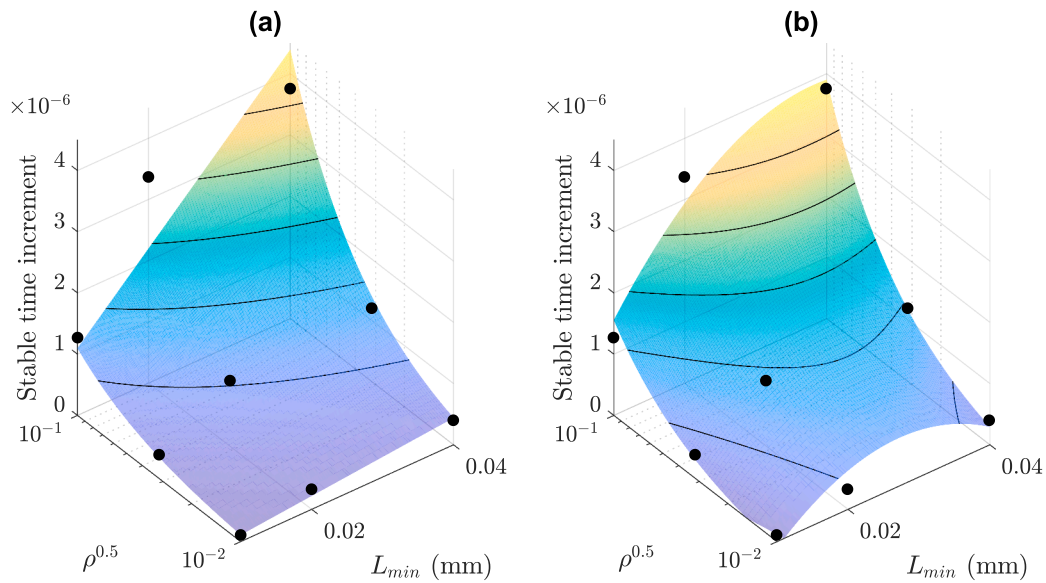
**Fig. 13.** *Stable time increment in Abaqus Explicit for the axisymmetric model of a notched tensile test.* Dots represent the stable time increment at the end of the step for each combination of numerical density ($\rho$) and minimum element size ($L_{min}$). Results are fitted to a function $\Delta\tau_1 = m_1\rho^{0.5}L_{min}$ in (a) and to a function $\Delta\tau_2 = m_2\rho L_{min}^2$ in (b). Regions that are fitted better by $\Delta\tau_1$ are governed by the mechanical stability whereas $\Delta\tau_2$ matches diffusion-controlled increments.
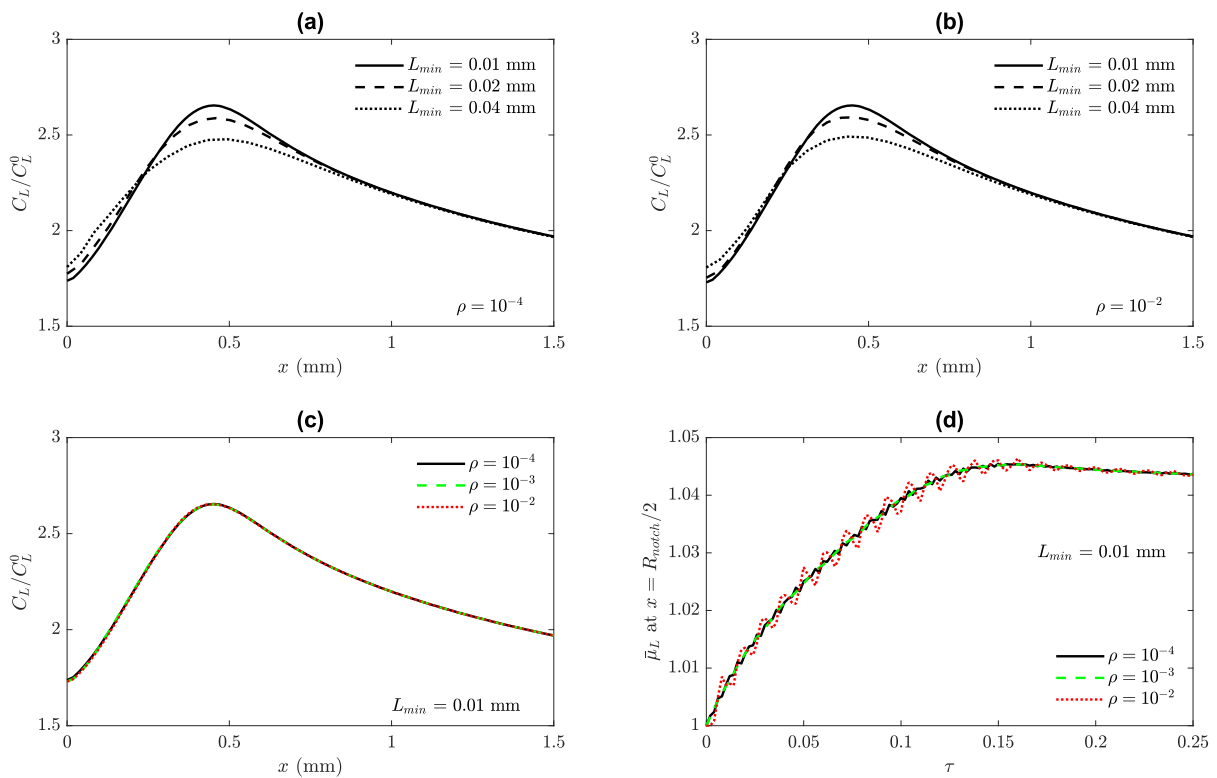


**Fig. 14.** *Influence of mesh and mass scaling on hydrogen distributions and normalised chemical potential.* In (a) and (b) three different element sizes are compared for two numerical densities. A need of mesh refinement is demonstrated but differences for finer meshes are small. The influence of numerical density on the final hydrogen distribution is negligible, as shown in (c), despite the numerical noise (d) observed for high densities ($\rho = 10^{-2}$) in the non-dimensional chemical potential at a distance $R_{notch}/2$ from the notch surface.

excessive mass scaling the stability is governed by the thermal-diffusion problem. The theoretical stability influence is numerically confirmed using a 2D axisymmetric example of hydrogen accumulation near a V-notch during straining. It has been demonstrated that the implementation strategy in ABAQUS Explicit adequately predicts stress-assisted hydrogen accumulation near the notch in reasonable computation times. In addition, the stress-dependent concentration at surfaces is naturally captured and simplifies boundary conditions.

A simulation of the same notched model problem has also demonstrated the capability of the framework for 3D models without code modifications. The simplicity of the rate-based formulation facilitates the applicability of the code to different element types. Linear

tetrahedrons result in numerical noise due to volumetric locking and thus results are not accurate. On the contrary, linear hexahedrons show stable responses and optimal computational costs. The present strategy is ideal to couple hydrogen transport (VUMATHT) with a user-defined material behaviour (VUMAT) and is expected to contribute to the development of hydrogen-informed damage models that usually rely on explicit schemes.

## CRediT authorship contribution statement

**A. Díaz:** Writing – original draft, Validation, Formal analysis, Software, Writing – review & editing, Methodology, Investigation, Data curation, Conceptualization. **J.M. Alegre:** Writing – review & editing, Supervision, Methodology, Project administration, Resources, Funding acquisition, Conceptualization. **I.I. Cuesta:** Writing – review & editing, Supervision, Resources, Project administration, Methodology, Funding acquisition, Conceptualization. **Z. Zhang:** Writing – review & editing, Methodology, Funding acquisition, Formal analysis, Conceptualization.

## Declaration of competing interest

The authors declare the following financial interests/personal relationships which may be considered as potential competing interests:

Andres Diaz reports financial support was provided by Spain Ministry of Science and Innovation. Andres Diaz reports financial support was provided by Junta de Castilla y León Consejería de Educación. If there are other authors, they declare that they have no known competing financial interests or personal relationships that could have appeared to influence the work reported in this paper.

## Data availability

Data will be made available on request.

## Acknowledgments

## Appendix A. Symbol abbreviations

| | |
|---|---|
| $b$ | crack opening displacement |
| $b_0$ | initial crack width |
| $c$ | diffusion coefficient term (Comsol) |
| $c_e$ | effective specific heat transfer ($\partial U/\partial t$) |
| $C_L$ | concentration in lattice sies |
| $C_L^0$ | equilibrium $C_L$ in the absence of stress. |
| $C_L^0$ | $C_L$ at a boundary. |
| $C_L^r$ | reference $C_L$ for non-dimensional modelling |
| $C_L^I$ | initial $C_L$ |
| $\overline{C}_L$ | non-dimensional lattice concentration: $C_L/C_L^r$ |
| $C_T$ | concentration in trapping sites |
| $D^*$ | operational diffusivity term |
| $D_L$ | lattice diffusivity |
| $D_L^r$ | lattice diffusivity normalised by $t_{load}$ |
| $d_a$ | Damping term (Comsol) |
| $E$ | Young's modulus |
| $E_B$ | binding energy of traps |
| $E_{In}$ | dissipated inelastic specific energy |
| $f$ | source term (Comsol) |
| $f_{H_2}$ | hydrogen fugacity |
| $\boldsymbol{I}$ | identity tensor |
| $\mathbf{J}_L$ | hydrogen flux vector |
| $J_L^B$ | hydrogen flux at a boundary |
| $K$ | hydrogen solubility |
| $K_I$ | loading stress intensity factor |
| $K_T$ | trapping constant |
| $k_{abs}, k_{des}$ | absorption and desorption constants for generalised boundary conditions |
| $k_e$ | effective conductivity (ABAQUS) |
| $L_{min}$ | minimum element length |
| $N_L$ | density of lattice sites |
| $N_T$ | density of trapping sites |
| $n$ | hardening exponent |
| $p_{H_2}$ | hydrogen pressure |
| $p_0$ | reference pressure |
| $R$ | constant of gases |
| $R_b$ | radius of the outer boundary layer |
| $r$ | heat source term (ABAQUS) |
| $r_p$ | heat source from plastic dissipation (ABAQUS) |
| $\mathscr{S}_H$ | boundary for hydrogen uptake |
| $T, T_0$ | temperature and uniform temperature value |
| $t$ | time |
| $t_{load}$ | loading time |

*(continued on next page)*

(*continued*)

| | |
|---|---|
| $U$ | internal thermal energy (ABAQUS) |
| $U_p$ | contribution of the plastic strain rate to $U$ |
| $u_x, u_y$ | displacements of the outer boundary layer |
| $\overline{V}_H$ | partial molar volume of hydrogen |
| $w_p$ | plastic work |
| $\boldsymbol{x}$ | spatial coordinates |
| $x$ | distance from the crack or notch tip |
| | *Greek symbols* |
| $\alpha$ | convection coefficient (Comsol) |
| $\boldsymbol{\Delta\varepsilon}$ | strain increment tensor |
| $\varepsilon_p$ | equivalent plastic strain |
| $\eta$ | inelastic heat fraction |
| $\theta$ | angle with the crack plane |
| $\theta_{ad}$ | coverage of adsorbed hydrogen |
| $\theta_L$ | occupancy of lattice sites |
| $\theta_T$ | occupancy of trapping sites |
| $\lambda, \mu$ | Lamé parameters |
| $\mu_{H_2}$ | chemical potential of $H_2$ |
| $\mu_L$ | chemical potential of hydrogen in lattice sites |
| $\mu_L^B$ | $\mu_L$ at a boundary |
| $\mu_L^0$ | $\mu_L$ in a reference state |
| $\mu_L^r$ | reference $\mu_L$ for non-dimensional modelling |
| $\mu_L^I$ | initial $\mu_L$ |
| $\overline{\mu}_L$ | non-dimensional chemical potential: $\mu_L/\mu_L^r$ |
| $\nu$ | Poisson's coefficient |
| $\xi_M, \xi_T$ | correction factors for mechanical and thermal stable increments |
| $\rho$ | numerical density |
| $\boldsymbol{\sigma}$ | Cauchy stress tensor |
| $\sigma_h$ | hydrostatic stress |
| $\sigma_h^B$ | $\sigma_h$ at a boundary |
| $\sigma_y$ | yield stress |
| $\sigma_y^0$ | initial yield stress |
| $\sigma_e$ | equivalent or von Mises stress |
| $\tau$ | non-dimensional time |
| $\Delta\tau$ | non-dimensional time increment |
| $\Delta\tau_M, \Delta\tau_T$ | mechanical and thermal stable increments of non-dimensional time |

## Appendix B. Derivation of concentration-based PDE

The chemical potential gradient is the thermodynamic driving force for diffusion. To obtain a concentration-based governing equation, $\nabla\mu_L$ is expressed as a function of lattice concentration, hydrostatic stress and temperature gradients by deriving Eq. (5):

$$\nabla\mu_L = \frac{RT}{C_L}\nabla C_L - \overline{V}_H\nabla\sigma_h + R\ln\left(\frac{C_L}{N_L}\right)\nabla T \tag{B.1}$$

Despite the implementation in the present paper only considers isothermal conditions, the term proportional to $\nabla T$ is also extended to illustrate its influence in the transport governing equation. Substituting $\nabla\mu_L$ into the flux expression (Eq. (3)), the mass balance is given by:

$$\frac{\partial C_L}{\partial t} + \frac{\partial C_T}{\partial t} = \nabla\cdot\left(D_L\nabla C_L - \frac{D_L C_L}{RT}\overline{V}_H\nabla\sigma_h + \frac{D_L C_L}{T}\ln\left(\frac{C_L}{N_L}\right)\nabla T\right) \tag{B.2}$$

For an isothermal analysis, $T = T_0$, the concentration-based governing equation is obtained:

$$\frac{\partial C_L}{\partial t} + \frac{\partial C_T}{\partial t} = \nabla\cdot\left(D_L\nabla C_L - \frac{D_L C_L}{RT_0}\overline{V}_H\nabla\sigma_h\right) \tag{B.3}$$

In Eq. (B.3), the trapping rate $\partial C_T/\partial t$ acts as a hydrogen sink and therefore it can be modelled as a source term. On the other hand, since the stress-dependent term is proportional to $C_L$ it can be regarded as a convective term that drifts ideal diffusion. In order to express $\partial C_T/\partial t$ as a function of $C_L$, thermodynamic equilibrium is assumed for the governing equation in next sections. Equilibrium between lattice and trapped hydrogen is expressed through the usual Oriani's relationship s [68]:

$$\frac{\theta_T}{1-\theta_T} = \frac{\theta_L}{1-\theta_L}K_T \tag{B.4}$$

where, the trap occupancy is defined as $\theta_T = C_T/N_T$, being $N_T$ the density of trapping sites. Similarly, the lattice occupancy $\theta_L = C_L/N_L$ where $N_L$ is the density of interstitial sites. The equilibrium constant depends on the binding energy, $E_B$:

$$K_T = \exp\left(\frac{E_B}{RT}\right) \tag{B.5}$$

Therefore, hydrogen concentration in trapping sites can be directly calculated from $C_L$. Assuming a low lattice occupancy, $\theta_L \ll 1$:

$$C_T = \frac{N_T}{1 + \frac{N_L}{K_T C_L}} \tag{B.6}$$

This form is here rearranged to avoid division by zero in empty regions:

$$C_T = N_T \frac{K_T C_L / N_L}{K_T C_L / N_L + 1} \tag{B.7}$$

And the rate of hydrogen trapping can be expressed, using the chain rule, as a function of $C_L$, $N_T$ and $T$ variations:

$$\frac{\partial C_T}{\partial t} = \frac{\partial C_T}{\partial C_L}\frac{\partial C_L}{\partial t} + \frac{\partial C_T}{\partial N_T}\frac{\partial \varepsilon_p}{\partial t} + \frac{\partial C_T}{\partial K_T}\frac{\partial K_T}{\partial T}\frac{\partial T}{\partial t} \tag{B.8}$$

In this derivation, the number of lattice sites, $N_L$, and the binding energy, $E_B$, are assumed to be uniform whereas $N_T$ increases as a function of plastic strain or dislocation density. Deriving each term from Eq. (B.8), the trapping rate term is expressed through $C_L$, $\varepsilon_p$ and $T$ rates:

$$\frac{\partial C_T}{\partial t} = \left(\frac{C_T(1-\theta_T)}{C_L}\right)\frac{\partial C_L}{\partial t} + \theta_T \frac{\partial N_T}{\partial \varepsilon_p}\frac{\partial \varepsilon_p}{\partial t} + \frac{C_T(1-\theta_T)E_B}{RT^2}\frac{\partial T}{\partial t} \tag{B.9}$$

The general hydrogen transport equation based on $C_L$ as the dependent variable is thus obtained substituting (B.9) into (B.3):

$$\left(1 + \frac{C_T(1-\theta_T)}{C_L}\right)\frac{\partial C_L}{\partial t} + \theta_T \frac{\partial N_T}{\partial \varepsilon_p}\frac{\partial \varepsilon_p}{\partial t} + \frac{C_T(1-\theta_T)E_B}{RT^2}\frac{\partial T}{\partial t} = \nabla\cdot\left(D_L\nabla C_L - \frac{D_L C_L}{RT}\overline{V}_H\nabla\sigma_h + \frac{D_L C_L}{T}\ln\left(\frac{C_L}{N_L}\right)\nabla T\right) \tag{B.10}$$

For an isothermal analysis, $T = T_0$:

$$\left(1 + \frac{C_T(1-\theta_T)}{C_L}\right)\frac{\partial C_L}{\partial t} + \theta_T \frac{\partial N_T}{\partial \varepsilon_p}\frac{\partial \varepsilon_p}{\partial t} = \nabla\cdot\left(D_L\nabla C_L - \frac{D_L C_L}{RT_0}\overline{V}_H\nabla\sigma_h\right) \tag{B.11}$$

## Appendix C. Derivation of chemical potential-based PDE

In this case, the chemical potential gradient does not need to be expanded because e $\mu_L$ is the dependent variable of the governing PDE. However, the $C_L$ rate term in the mass balance must be expressed as a function of the $\mu_L$ rate. Applying the chain rule to Eq. (5):

$$\frac{\partial \mu_L}{\partial t} = \frac{\partial \mu_L}{\partial C_L}\frac{\partial C_L}{\partial t} + \frac{\partial \mu_L}{\partial \sigma_h}\frac{\partial \sigma_h}{\partial t} + \frac{\partial \mu_L}{\partial T}\frac{\partial T}{\partial t} \tag{C.1}$$

After the derivation of terms, the chemical potential rate can be expressed as:

$$\frac{\partial \mu_L}{\partial t} = \frac{RT}{C_L}\frac{\partial C_L}{\partial t} - \overline{V}_H\frac{\partial \sigma_h}{\partial t} + R\ln\left(\frac{C_L}{N_L}\right)\frac{\partial T}{\partial t} \tag{C.2}$$

The term $\partial C_L / \partial t$ is then isolated,

$$\frac{\partial C_L}{\partial t} = \frac{C_L}{RT}\frac{\partial \mu_L}{\partial t} + \frac{C_L}{RT}\overline{V}_H\frac{\partial \sigma_h}{\partial t} - \frac{C_L}{T}\ln\left(\frac{C_L}{N_L}\right)\frac{\partial T}{\partial t} \tag{C.3}$$

and substituted in Eq. (1):

$$D^*\frac{C_L}{RT}\frac{\partial \mu_L}{\partial t} = \nabla\cdot\left(D_L\frac{C_L}{RT}\nabla\mu_L\right) - D^*\frac{C_L}{RT}\overline{V}_H\frac{\partial \sigma_h}{\partial t} - \theta_T\frac{dN_T}{d\varepsilon_p}\frac{\partial \varepsilon_p}{\partial t} + \left(D^*\frac{C_L}{T}\ln\frac{C_L}{N_L} + \frac{C_T(1-\theta_T)E_B}{RT^2}\right)\frac{\partial T}{\partial t} \tag{C.4}$$

where, the flux term $\mathbf{J}_L$ is not expanded but expressed directly as a function of $\nabla\mu_L$ (Eq. (3)). For an isothermal analysis, $T = T_0$, the final governing equation is:

$$D^*\frac{C_L}{RT_0}\frac{\partial \mu_L}{\partial t} = \nabla\cdot\left(D_L\frac{C_L}{RT_0}\nabla\mu_L\right) - D^*\frac{C_L}{RT_0}\overline{V}_H\frac{\partial \sigma_h}{\partial t} - \theta_T\frac{dN_T}{d\varepsilon_p}\frac{\partial \varepsilon_p}{\partial t} \tag{C.5}$$

## Appendix D. Boundary and initial conditions for non-dimensional modelling based on the chemical potential

In a concentration-based model the initial and boundary conditions are straightforward: $C_L^I$ and $C_L^B$. For the non-dimensional chemical potential-based PDE, these must be translated into $\overline{\mu}_L^I$ and $\overline{\mu}_L^B$, defined as:

$$\overline{\mu}_L^I = \overline{\mu}_L(\mathbf{x}, t=0) = \frac{\mu_L^0 + RT_0\ln\left(C_L^I/N_L\right)}{\mu_L^0 + RT_0\ln\left(C_L^r/N_L\right)} \tag{D.3}$$

$$\overline{\mu}_L^B = \overline{\mu}_L(\mathbf{x} \in \mathscr{S}_H, t) = \frac{\mu_L^0 + RT_0\ln\left(C_L^0/N_L\right)}{\mu_L^0 + RT_0\ln\left(C_L^r/N_L\right)} \tag{D.4}$$

The hydrostatic stress does not need to be included in the boundary condition (D.4) because the stress influence is captured through the transformation into $C_L^B$:

$$C_L^B = N_L \exp\left(\frac{\overline{\mu}_L^B \mu_L^r - \mu_L^0 + \overline{V}_H \sigma_h}{RT_0}\right) \tag{D.5}$$

The analysed examples in Sections 5–7 simulate a saturated material with a continuous external hydrogen source and thus $C_L^r = C_L^0 = C_L^I$. Therefore, $\overline{\mu}_L^I = \overline{\mu}_L^B = 1$. To simulate an empty material or hydrogen egress through a surface, i.e. $C_L^I = 0$ or $C_L^0 = 0$, it must be noted that a zero concentration does not correspond to a zero chemical potential. A non-dimensional empty potential $\overline{\mu}_e$ is here defined by assuming a very low $\theta_L$ value.

$$\overline{\mu}_e = \frac{\mu_L^0 + RT_0 \ln(\theta_L \to 0)}{\mu_L^0 + RT_0 \ln\left(C_L^r/N_L\right)} \tag{D.1}$$

Alternatively, a very high positive value or very negative value can be directly fixed depending on the reference chemical potential and reference concentration:

$$\left|\frac{\mu_L^0}{RT\ln\left(C_L^r/N_L\right)}\right| \left\langle 1, \ \overline{\mu}_e \to \infty \ \left|\frac{\mu_L^0}{RT\ln\left(C_L^r/N_L\right)}\right| \right\rangle 1, \ \overline{\mu}_e \to -\infty \tag{D.2}$$

The possible situations and their corresponding initial and boundary conditions are summarised in Table D.1. The situation where a non-zero $C_L^0$ is different than the non-zero $C_L^I$, which is not included in Table D.1, requires the determination of $\overline{\mu}_L^B = \overline{\mu}_L(\theta_L = \theta_L^0)$.

**Table D.1**
Assignment of initial and boundary conditions for the non-dimensional governing equation based on the chemical potential.

|  |  | $C_L^I = 0$ | $C_L^I > 0$ |
|---|---|---|---|
| $C_L^0 = 0$ | Situation | No hydrogen | Internal hydrogen: $C_L^r = C_L^I$ |
|  | ICs | – | $\overline{\mu}_L^I = 1$ |
|  | BCs | – | $\overline{\mu}_L^B = \overline{\mu}_e$ |
| $C_L^0 > 0$ | Situation | External hydrogen: $C_L^r = C_L^0$ | Saturation: $C_L^r = C_L^I = C_L^0$ |
|  | ICs | $\overline{\mu}_L^I = \overline{\mu}_e$ | $\overline{\mu}_L^I = 1$ |
|  | BCs | $\overline{\mu}_L^B = 1$ | $\overline{\mu}_L^B = 1$ |

## References

[1] Dwivedi SK, Vishwakarma M. Hydrogen embrittlement in different materials: a review. Int J Hydrogen Energy 2018;43:21603–16. https://doi.org/10.1016/J.IJHYDENE.2018.09.201.

[2] Campari A, Ustolin F, Alvaro A, Paltrinieri N. A review on hydrogen embrittlement and risk-based inspection of hydrogen technologies. Int J Hydrogen Energy 2023; 48:35316–46. https://doi.org/10.1016/J.IJHYDENE.2023.05.293.

[3] Oriani RA. A mechanistic theory of hydrogen embrittlement of steels. Berichte der Bunsengesellschaft für physikalische Chemie 1972;76:848–57. https://doi.org/10.1002/BBPC.19720760864.

[4] Takahashi Y, Kondo H, Asano R, et al. Direct evaluation of grain boundary hydrogen embrittlement: a micro-mechanical approach. Mater Sci Eng A 2016;661: 211–6. https://doi.org/10.1016/J.MSEA.2016.03.035.

[5] Beachem CD. A new model for hydrogen-assisted cracking (hydrogen "embrittlement"). Metall Trans 1972;3:441–55.

[6] Martin ML, Dadfarnia M, Nagao A, et al. Enumeration of the hydrogen-enhanced localized plasticity mechanism for hydrogen embrittlement in structural materials. Acta Mater 2019;165:734–50. https://doi.org/10.1016/J.ACTAMAT.2018.12.014.

[7] Lynch S. Discussion of some recent literature on hydrogen-embrittlement mechanisms: addressing common misunderstandings. Corros Rev 2019;37:377–95. https://doi.org/10.1515/CORRREV-2019-0017/MACHINEREADABLECITATION/RIS.

[8] Lynch SP. Progress towards understanding mechanisms of hydrogen embrittlement and stress corrosion cracking. Corrosion. NACE International; 2007.

[9] Koyama M, Rohwerder M, Tasan CC, et al. Recent progress in microstructural hydrogen mapping in steels: quantification, kinetic analysis, and multi-scale characterisation. Mater Sci Technol 2017;33:1481–96. https://doi.org/10.1080/02670836.2017.1299276.

[10] Martínez-Pañeda E, Harris ZD, Fuentes-Alonso S, et al. On the suitability of slow strain rate tensile testing for assessing hydrogen embrittlement susceptibility. Corros Sci 2020;163:108291. https://doi.org/10.1016/J.CORSCI.2019.108291.

[11] Vadillo G, Zaera R, Fernández-Sáez J. Consistent integration of the constitutive equations of Gurson materials under adiabatic conditions. Comput Methods Appl Mech Eng 2008;197:1280–95. https://doi.org/10.1016/J.CMA.2007.11.008.

[12] Jiang W, Li Y, Su J. Modified GTN model for a broad range of stress states and application to ductile fracture. Eur J Mech A/Solids 2016;57:132–48. https://doi.org/10.1016/J.EUROMECHSOL.2015.12.009.

[13] Diehl T. On using a penalty-based cohesive-zone finite element approach, Part I: elastic solution benchmarks. Int J Adhes Adhes 2008;28:237–55. https://doi.org/10.1016/J.IJADHADH.2007.06.003.

[14] Zavattieri PD. Modeling of crack propagation in thin-walled structures using a cohesive model for shell elements. J Appl Mech 2006;73:948–58. https://doi.org/10.1115/1.2173286.

[15] Wang T, Ye X, Liu Z, et al. A phase-field model of thermo-elastic coupled brittle fracture with explicit time integration. Comput Mech 2020;65:1305–21. https://doi.org/10.1007/S00466-020-01820-6/TABLES/6.

[16] Zecevic M, Cawkwell MJ, Ramos KJ, Luscher DJ. An implementation of the phase-field model based on coupled thermomechanical finite element solvers for large-strain twinning, explicit dynamic fracture, and the classical Stefan problem. Model Simul Mat Sci Eng 2020;28:055002. https://doi.org/10.1088/1361-651X/AB8357.

[17] Zhou J, Mu Y, Wang B. A damage-coupled unified viscoplastic constitutive model for prediction of forming limits of 22MnB5 at high temperatures. Int J Mech Sci 2017;133:457–68. https://doi.org/10.1016/J.IJMECSCI.2017.09.006.

[18] Lee SW, Pourboghrat F. Finite element simulation of the punchless piercing process with Lemaitre damage model. Int J Mech Sci 2005;47:1756–68. https://doi.org/10.1016/J.IJMECSCI.2005.06.009.

[19] Ben Said L, J Mars, Wali M, Dammak F. Numerical prediction of the ductile damage in single point incremental forming process. Int J Mech Sci 2017;131–132:546–58. https://doi.org/10.1016/J.IJMECSCI.2017.08.026.

[20] Ghorbel O, Mars J, Koubaa S, et al. Coupled anisotropic plasticity-ductile damage: modeling, experimental verification, and application to sheet metal forming simulation. Int J Mech Sci 2019;150:548–60. https://doi.org/10.1016/J.IJMECSCI.2018.10.044.

[21] Storvik E, Both JW, Sargado JM, et al. An accelerated staggered scheme for variational phase-field models of brittle fracture. Comput Methods Appl Mech Eng 2021;381:113822. https://doi.org/10.1016/J.CMA.2021.113822.

[22] Hai L, Zhang H, Wriggers P, et al. 3D concrete fracture simulations using an explicit phase field model. Int J Mech Sci 2024;265:108907. https://doi.org/10.1016/J.IJMECSCI.2023.108907.

[23] Ren HL, Zhuang XY, Anitescu C, Rabczuk T. An explicit phase field method for brittle dynamic fracture. Comput Struct 2019;217:45–56. https://doi.org/10.1016/J.COMPSTRUC.2019.03.005.

[24] Zhang P, Hu X, Bui TQ, Yao W. Phase field modeling of fracture in fiber reinforced composite laminate. Int J Mech Sci 2019;161–162:105008. https://doi.org/10.1016/J.IJMECSCI.2019.07.007.

[25] Wang T, Ye X, Liu Z, et al. Modeling the dynamic and quasi-static compression-shear failure of brittle materials by explicit phase field method. Comput Mech 2019;64:1537–56. https://doi.org/10.1007/S00466-019-01733-Z/FIGURES/28.

[26] Ziaei-Rad V, Shen Y. Massive parallelization of the phase field formulation for crack propagation with time adaptivity. Comput Methods Appl Mech Eng 2016; 312:224–53. https://doi.org/10.1016/J.CMA.2016.04.013.

[27] Yu H, Olsen JS, Alvaro A, et al. Hydrogen informed Gurson model for hydrogen embrittlement simulation. Eng Fract Mech 2019;106542. https://doi.org/10.1016/J.ENGFRACMECH.2019.106542.

[28] Depraetere R, De Waele W, Hertelé S. Fully-coupled continuum damage model for simulation of plasticity dominated hydrogen embrittlement mechanisms. Comput Mater Sci 2021;200:110857. https://doi.org/10.1016/J.COMMATSCI.2021.110857.

[29] Scheider I, Pfuff M, Dietzel W. Simulation of hydrogen assisted stress corrosion cracking using the cohesive model. Eng Fract Mech 2008;75:4283–91. https://doi.org/10.1016/j.engfracmech.2007.10.002.

[30] Moriconi C, Hénaff G, Halm D. Cohesive zone modeling of fatigue crack propagation assisted by gaseous hydrogen in metals. Int J Fatigue 2014;68:56–66. https://doi.org/10.1016/j.ijfatigue.2014.06.007.

[31] Jemblie L, Olden V, Akselsen OM. A coupled diffusion and cohesive zone modelling approach for numerically assessing hydrogen embrittlement of steel structures. Int J Hydrogen Energy 2017;42:11980–95. https://doi.org/10.1016/J.IJHYDENE.2017.02.211.

[32] Golahmar A, Kristensen PK, Niordson CF, Martínez-Pañeda E. A phase field model for hydrogen-assisted fatigue. Int J Fatigue 2022;154:106521. https://doi.org/10.1016/J.IJFATIGUE.2021.106521.

[33] Martínez-Pañeda E, Golahmar A, Niordson CF. A phase field formulation for hydrogen assisted cracking. Comput Methods Appl Mech Eng 2018;342:742–61. https://doi.org/10.1016/J.CMA.2018.07.021.

[34] Mandal TK, Nguyen VP, Wu JY. Comparative study of phase-field damage models for hydrogen assisted cracking. Theor Appl Fracture Mech 2021;111:102840. https://doi.org/10.1016/J.TAFMEC.2020.102840.

[35] Yu H, Olsen JS, He J, Zhang Z. Hydrogen-microvoid interactions at continuum scale. Int J Hydrogen Energy 2018;43:10104–28. https://doi.org/10.1016/J.IJHYDENE.2018.04.064.

[36] Serebrinsky S, Carter EA, Ortiz M. A quantum-mechanically informed continuum model of hydrogen embrittlement. J Mech Phys Solids 2004;52:2403–30.

[37] Kristensen PK, Niordson CF, Martínez-Pañeda E. A phase field model for elastic-gradient-plastic solids undergoing hydrogen embrittlement. J Mech Phys Solids 2020;143:104093. https://doi.org/10.1016/J.JMPS.2020.104093.

[38] Yu H, Olsen JS, Alvaro A, et al. A uniform hydrogen degradation law for high strength steels. Eng Fract Mech 2016;157:56–71. https://doi.org/10.1016/j.engfracmech.2016.02.001.

[39] Mandal TK, Parker J, Gagliano M, Martínez-Pañeda E. Computational predictions of weld structural integrity in hydrogen transport pipelines. Int J Hydrogen Energy 2024. https://doi.org/10.1016/J.IJHYDENE.2024.01.258.

[40] Di Leo CV, Anand L. Hydrogen in metals: a coupled theory for species diffusion and large elastic–plastic deformations. Int J Plast 2013;43:42–69. https://doi.org/10.1016/j.ijplas.2012.11.005.

[41] Díaz A, Alegre JM, Cuesta II. Coupled hydrogen diffusion simulation using a heat transfer analogy. Int J Mech Sci 2016;115–116. https://doi.org/10.1016/j.ijmecsci.2016.07.020.

[42] Fernández-Sousa R, Betegón C, Martínez-Pañeda E. Analysis of the influence of microstructural traps on hydrogen assisted fatigue. Acta Mater 2020. https://doi.org/10.1016/j.actamat.2020.08.030.

[43] Liu Q, Atrens AD, Shi Z, et al. Determination of the hydrogen fugacity during electrolytic charging of steel. Corros Sci 2014;87:239–58. https://doi.org/10.1016/J.CORSCI.2014.06.033.

[44] Turnbull A. Perspectives on hydrogen uptake, diffusion and trapping. Int J Hydrogen Energy 2015. https://doi.org/10.1016/j.ijhydene.2015.06.147.

[45] Peral L, Díaz A, Alegre J, Cuesta I. Hydrogen uptake and diffusion kinetics in a quenched and tempered low carbon steel: experimental and numerical study. Int J Hydrogen Energy 2023. https://doi.org/10.1016/J.IJHYDENE.2023.05.286.

[46] Marchi CS, Somerday BP, Robinson SL. Permeability, solubility and diffusivity of hydrogen isotopes in stainless steels at high gas pressures. Int J Hydrogen Energy 2007;32:100–16. https://doi.org/10.1016/j.ijhydene.2006.05.008.

[47] M. H. Koren E, Hagen C, Wang D, et al. Experimental comparison of gaseous and electrochemical hydrogen charging in X65 pipeline steel using the permeation technique Corros Sci 2023;215:111025. https://doi.org/10.1016/J.CORSCI.2023.111025.

[48] Sofronis P, McMeeking RM. Numerical analysis of hydrogen transport near a blunting crack tip. J Mech Phys Solids 1989;37:317–50. https://doi.org/10.1016/0022-5096(89)90002-1.

[49] Martínez-Pañeda E, del Busto S, Niordson CF, Betegón C. Strain gradient plasticity modeling of hydrogen diffusion to the crack tip. Int J Hydrogen Energy 2016;41:10265–74. https://doi.org/10.1016/J.IJHYDENE.2016.05.014.

[50] Montella C. Discussion on permeation transients in terms of insertion reaction mechanism and kinetics. J Electroanal Chem 1999;465:37–50. https://doi.org/10.1016/S0022-0728(99)00051-0.

[51] Turnbull A. Modelling of environment assisted cracking. Corros Sci 1993;34:921–60. https://doi.org/10.1016/0010-938X(93)90072-O.

[52] Turnbull A, Ferriss DH, Anzai H. Modelling of the hydrogen distribution at a crack tip. Mater Sci Eng A 1996;206:1–13. https://doi.org/10.1016/0921-5093(95)09897-6.

[53] Martínez-Pañeda E, Díaz A, Wright L, Turnbull A. Generalised boundary conditions for hydrogen transport at crack tips. Corros Sci 2020;173:108698. https://doi.org/10.1016/j.corsci.2020.108698.

[54] Krom AHM, Koers RWJ, Bakker A. Hydrogen transport near a blunting crack tip. J Mech Phys Solids 1999;47:971–92.

[55] Dadfarnia M, Sofronis P, Neeraj T. Hydrogen interaction with multiple traps: can it be used to mitigate embrittlement? Int J Hydrogen Energy 2011;36:10141–8. https://doi.org/10.1016/j.ijhydene.2011.05.027.

[56] Kotake H, Matsumoto R, Taketomi S, Miyazaki N. Transient hydrogen diffusion analyses coupled with crack-tip plasticity under cyclic loading. Int J Press Vessels Pip 2008;85:540–9. https://doi.org/10.1016/j.ijpvp.2008.02.002.

[57] Lu X, Díaz A, Ma J, et al. The effect of plastic deformation on hydrogen diffusion in nickel Alloy 625. Scr Mater 2023;226:115210. https://doi.org/10.1016/J.SCRIPTAMAT.2022.115210.

[58] Dadfarnia M, Martin ML, Nagao A, et al. Modeling hydrogen transport by dislocations. J Mech Phys Solids 2014;78:511–25. https://doi.org/10.1016/j.jmps.2015.03.002.

[59] Díaz A, Cuesta II, Rodríguez C, Alegre JM. Influence of non-homogeneous microstructure on hydrogen diffusion and trapping simulations near a crack tip in a welded joint. Theor Appl Fract Mech 2021;112:102879. https://doi.org/10.1016/J.TAFMEC.2020.102879.

[60] Toribio J, Kharin V. A generalised model of hydrogen diffusion in metals with multiple trap types. Philos Mag 2015;1–23. https://doi.org/10.1080/14786435.2015.1079660.

[61] Ågren J. The Onsager reciprocity relations revisited. J Phase Equilibria Diffus 2022;43:640–7. https://doi.org/10.1007/S11669-022-00951-Y/TABLES/2.

[62] McLellan AG. Non-hydrostatic thermodynamics of chemical systems. Proc R Soc Lond A Math Phys Sci 1970;314(1518):443–55.

[63] Li JCM, Oriani RA. The thermodynamics of stressed solids. Zeitschrift fur Physikalische Chemie 1966;49:271–90. https://doi.org/10.1524/ZPCH.1966.49.3_5.271/MACHINEREADABLECITATION/RIS.

[64] Drexler A, He S, Razumovskiy V, et al. Verification of the generalised chemical potential for stress-driven hydrogen diffusion in nickel. Philos Mag Lett 2020;100:513–23. https://doi.org/10.1080/09500839.2020.1808253.

[65] Kirchheim R, Hirth JP. Stress and solubility for solutes with asymmetrical distortion fields. Acta Metall 1987;35:2899–903. https://doi.org/10.1016/0001-6160(87)90288-4.

[66] Hirth J. Effects of hydrogen on the properties of iron and steel. Metall Trans A 1980;11:861–90. https://doi.org/10.1007/BF02654700.

[67] Luo F, Liu Q, Huang J, et al. Effects of lattice strain on hydrogen diffusion, trapping and escape in bcc iron from *ab-initio* calculations. Int J Hydrogen Energy 2023;48:8198–215. https://doi.org/10.1016/J.IJHYDENE.2022.11.206.

[68] Oriani RA. The diffusion and trapping of hydrogen in steel. Acta Metall 1970;18:147–57. https://doi.org/10.1016/0001-6160(70)90078-7.

[69] McNabb A, Foster PK. A new analysis of the diffusion of hydrogen in iron and ferritic steels. Trans Metall Soc AIME 1963;227:618–27. https://citeulike-article-id:4956272.

[70] Wei F-G, Enomoto M, Tsuzaki K. Applicability of the Kissinger's formula and comparison with the McNabb–Foster model in simulation of thermal desorption spectrum. Comput Mater Sci 2012;51:322–30. https://doi.org/10.1016/J.COMMATSCI.2011.07.009.

[71] Kanayama H, Ndong-Mefane S, Ogino M, Miresmaeili R. Reconsideration of the hydrogen diffusion model using the McNabb-Foster formulation. Mem Faculty Eng Kyushu Univ 2009;69:149–61.

[72] Charles Y, Mougenot J, Gaspérini M. Effect of transient trapping on hydrogen transport near a blunting crack tip. Int J Hydrogen Energy 2021;46:10995–1003. https://doi.org/10.1016/J.IJHYDENE.2020.12.155.

[73] Díaz A, Cuesta II, Martínez-Pañeda E, Alegre JM. Influence of charging conditions on simulated temperature-programmed desorption for hydrogen in metals. Int J Hydrogen Energy 2020;45:23704–20. https://doi.org/10.1016/j.ijhydene.2020.05.192.

[74] Benannoune S, Charles Y, Mougenot J, Gaspérini M. Numerical simulation of the transient hydrogen trapping process using an analytical approximation of the McNabb and Foster equation. Int J Hydrogen Energy 2018;43:9083–93. https://doi.org/10.1016/J.IJHYDENE.2018.03.179.

[75] Hageman T, Martínez-Pañeda E. A phase field-based framework for electro-chemo-mechanical fracture: crack-contained electrolytes, chemical reactions and stabilisation. Comput Methods Appl Mech Eng 2023;415:116235. https://doi.org/10.1016/J.CMA.2023.116235.

[76] Kumnick AJ, Johnson HH. Deep trapping states for hydrogen in deformed iron. Acta Metall 1980;28:33–9. https://doi.org/10.1016/0001-6160(80)90038-3.

[77] Espeseth V, Morin D, Børvik T, Hopperstad OS. A gradient-based non-local GTN model: explicit finite element simulation of ductile damage and fracture. Eng Fract Mech 2023;289:109442. https://doi.org/10.1016/J.ENGFRACMECH.2023.109442.

[78] Martínez-Pañeda E, Fuentes-Alonso S, Betegón C. Gradient-enhanced statistical analysis of cleavage fracture. Eur J Mech A/Solids 2019;77:103785. https://doi.org/10.1016/J.EUROMECHSOL.2019.05.002.

[79] Bažant ZP, Vorel J. Energy-conservation error due to use of green-naghdi objective stress rate in commercial finite-element codes and its compensation. J Appl Mech 2014;81. https://doi.org/10.1115/1.4024411/370299. Transactions ASME.

[80] Knysh P, Korkolis YP. Determination of the fraction of plastic work converted into heat in metals. Mech Mater 2015;86:71–80. https://doi.org/10.1016/J.MECHMAT.2015.03.006.

[81] Navidtehrani Y, Betegón C, Martínez-Pañeda E. A simple and robust Abaqus implementation of the phase field fracture method. Appl Eng Sci 2021;6:100050. https://doi.org/10.1016/J.APPLES.2021.100050.

[82] Taha A, Sofronis P. A micromechanics approach to the study of hydrogen transport and embrittlement. Eng Fract Mech 2001;68:803–37. https://doi.org/10.1016/S0013-7944(00)00126-0.

[83] Dadfarnia M, Sofronis P, Somerday BP, Robertson IM. On the small scale character of the stress and hydrogen concentration fields at the tip of an axial crack in steel pipeline: effect of hydrogen-induced softening on void growth. Int J Mater Res 2008;99:557–70. https://doi.org/10.3139/146.101674.

[84] Segurado J, Lebensohn RA, Llorca J, Tomé CN. Multiscale modeling of plasticity based on embedding the viscoplastic self-consistent formulation in implicit finite elements. Int J Plast 2012;28:124–40. https://doi.org/10.1016/J.IJPLAS.2011.07.002.